AGU PUBLICATIONS

Water Resources Research

RESEARCH ARTICLE
10.1002/2016WR018704

Key Points:
- Reconstructed snow water equivalent is verified with spatial snow measurements from the Airborne Snow Observatory
- Reconstruction relies only on remotely sensed data and outperformed SNODAS and spatial interpolation from snow pillows
- Two reconstruction models tested comprise a full energy balance model and a net radiation plus degree-day model

Correspondence to:
E. H. Bair,
nbair@eri.ucsb.edu

Citation:
Bair, E. H., K. Rittger, R. E. Davis, T. H. Painter, and J. Dozier (2016), Validating reconstruction of snow water equivalent in California's Sierra Nevada using measurements from the NASA Airborne Snow Observatory, *Water Resour. Res.*, *52*, 8437–8460, doi:10.1002/2016WR018704.

Received 29 JAN 2016
Accepted 11 OCT 2016
Accepted article online 13 OCT 2016
Published online 9 NOV 2016

Validating reconstruction of snow water equivalent in California's Sierra Nevada using measurements from the NASA Airborne Snow Observatory

Edward H. Bair[1], Karl Rittger[2], Robert E. Davis[3], Thomas H. Painter[4], and Jeff Dozier[5]

[1]Earth Research Institute, University of California, Santa Barbara, California, USA, [2]National Snow and Ice Data Center, Boulder, Colorado, USA, [3]US Army Corps of Engineers Cold Regions Research and Engineering Laboratory, Hanover, New Hampshire, USA, [4]Jet Propulsion Laboratory, California Institute of Technology, Pasadena, California, USA, [5]Bren School of Environmental Science and Management, University of California, Santa Barbara, California, USA

Abstract Accurately estimating basin-wide snow water equivalent (SWE) is the most important unsolved problem in mountain hydrology. Models that rely on remotely sensed inputs are especially needed in ranges with few surface measurements. The NASA Airborne Snow Observatory (ASO) provides estimates of SWE at 50 m spatial resolution in several basins across the Western U.S. during the melt season. Primarily, water managers use this information to forecast snowmelt runoff into reservoirs; another impactful use of ASO measurements lies in validating and improving satellite-based snow estimates or models that can scale to whole mountain ranges, even those without ground-based measurements. We compare ASO measurements from 2013 to 2015 to four methods that estimate spatially distributed SWE: two versions of a SWE reconstruction method, spatial interpolation from snow pillows and courses, and NOAA's Snow Data Assimilation System (SNODAS). SWE reconstruction downscales energy forcings to compute potential melt, then multiplies those values by satellite-derived estimates of fractional snow-covered area to calculate snowmelt. The snowpack is then built in reverse from the date the snow is observed to disappear. The two SWE reconstruction models tested include one that employs an energy balance calculation of snowmelt, and one that combines net radiation and degree-day approaches to estimate melt. Our full energy balance model, without ground observations, performed slightly better than spatial interpolation from snow pillows, having no systematic bias and 26% mean absolute error when compared to SWE from ASO. Both reconstruction models and interpolation were more accurate than SNODAS.

1. Introduction

Accurately estimating basin-wide snow water equivalent (SWE) is the most important unsolved problem in mountain hydrology [*Dozier et al.*, 2016]. Worldwide, mountain snowmelt supports at least a billion people, and in the mountains themselves, snowmelt provides soil moisture late into the melt season. The need for methods that rely on remotely sensed inputs is especially prevalent over the world's biggest mountain ranges, where rugged topography and deep snow make extant methods of directly sensing SWE unreliable [*Lettenmaier et al.*, 2015] and where the heterogeneous distribution of snow causes measurements from surface networks to sometimes misrepresent the surrounding area [*Molotch and Bales*, 2005]. The need arises, therefore, to validate measurements and models of spatially distributed SWE with independent estimates of spatially distributed SWE. The goals of this paper are to construct such a validation chain.

1. The new NASA Airborne Snow Observatory (ASO) provides measurements of snow depth at fine spatial resolution, and SWE can be derived by multiplying depth by measured or modeled snow density [*Painter et al.*, 2016]. However, ASO can acquire data only over areas accessible to aircraft, and with spatial coverage and temporal frequency limited logistically.
2. SWE reconstruction [*Martinec and Rango*, 1981] is a promising technique for estimating snow water equivalent over large basins and whole mountain ranges. It involves building a snowpack in reverse, from melt-out back to peak accumulation, from estimates of melt energy and snow-covered area. With improvements in measuring snow-covered area and modeling snowmelt, we show that SWE reconstruction compares well with measurements from ASO.

3. Two other methods of estimating spatially distributed SWE—spatial interpolation from snow pillows combined with snow-covered area [*Fassnacht et al*., 2003] and NOAA's Snow Data Assimilation System [SNODAS, *Barrett*, 2003]—are less accurate than reconstruction. Among these two methods, SNODAS is less accurate than interpolation.

In this study, we validate two versions of a SWE reconstruction model with ASO data acquired from 2013 through 2015 in the upper Tuolumne River Basin in California's Sierra Nevada. We also validate ASO's accuracy in mapping snow by comparison with WorldView-3 imagery acquired on the same day as an ASO flight over the Kings River Basin. One reconstruction model uses a full energy balance model to calculate snowmelt; it uses remotely sensed snow albedo adjusted for light absorbing impurities, it uses accurate daily MODIS fractional snow-covered area (f_{SCA}) from a time-space smoothing method, it accounts for ephemeral (appears and disappears) snow, and it solves the energy balance for snow surface temperature. The second reconstruction model implements a net radiation/restricted degree-day approach [*Brubaker et al*., 1996].

Given the needs outlined, we utilize ASO validation data to illustrate that a model with explicit treatment of energy balance terms—i.e., snow albedo, f_{SCA}, snow surface temperature—yields accurate basin-wide SWE estimates. Such reconstructions can be implemented over large areas, with the caveat that the SWE can be calculated only from the end of the snow season back to the time of peak accumulation.

2. Background

2.1. Airborne Snow Observatory

A new project from NASA's Jet Propulsion Laboratory, the Airborne Snow Observatory (ASO) provides basin-wide estimates of snow water equivalent [*Painter et al*., 2016]. From an airplane with a scanning lidar altimeter, snow depths are measured as the differences between elevations of snow-free land in the summer and snow-covered land in the winter and spring. The snow's spectral properties are concurrently measured with an imaging spectrometer on the same platform. Using modeled and manually measured snow density, SWE is modeled as the product of depth $\times$ density. As standard products, ASO provides snow depth, SWE, and snow albedo at 3–50 m spatial resolution. These SWE retrievals have been used to provide operational runoff forecasts that are more accurate than from ground-based measurements alone [*McGurk and Painter*, 2014].

Another impactful use of ASO SWE measurements lies in validating and improving satellite-based SWE estimates, which can be used over whole mountain ranges and in austere regions with no ground-based snow or water data. Further, the ASO data address deficiencies of previously used verification data by offering SWE at fine spatial resolution. The main source of uncertainty in SWE has been reduced to only snow density, which varies 3$\times$ less than depth spatially [*López-Moreno et al*., 2013], but does vary in systematic ways that may affect the calculation of SWE. Generally, densities are lower at higher elevations and on slopes that receive less radiation [*Wetlaufer et al*., 2016].

2.2. SWE Reconstruction

Investigators have employed reconstruction to model SWE in large basins in ranges including the Rocky Mountains [*Molotch and Margulis*, 2008; *Molotch*, 2009; *Jepsen et al*., 2012] and the Sierra Nevada [*Cline et al*., 1998; *Guan et al*., 2013; *Girotto et al*., 2014; *Rittger et al*., 2016]. The main advantage of reconstruction is that it provides spatially resolved SWE estimates without the need for extensive ground-based observations. With advances in modern computing, reconstruction can be performed over whole mountain ranges at high-resolution spanning decades of time. For example, reconstructed estimates of peak SWE for the entire Sierra Nevada USA at 100 m resolution from 2000 to 2011 are now available [*Rittger et al*., 2016]. The disadvantages are that reconstruction can only be calculated retroactively after snow disappears, that it is only valid for the melt season, that persistent cloud cover can obscure the snow's date of disappearance, and that it is only suitable for areas with little accumulation during the melt season.

Reconstruction models range in spatial resolution from 30 m to 1 km. The tradeoff in spatial resolution is temporal resolution. For instance, accurate f_{SCA} values at 30 m from Landsat [e.g., *Rosenthal and Dozier*, 1996] are only available every 16 days, and those days may be cloudy, thereby protracting gaps between clear acquisitions and increasing model error [*Girotto et al*., 2014]. In contrast, the Moderate Resolution Imaging Spectrometer (MODIS) provides global daily coverage, but at $\sim$500 m resolution, which is

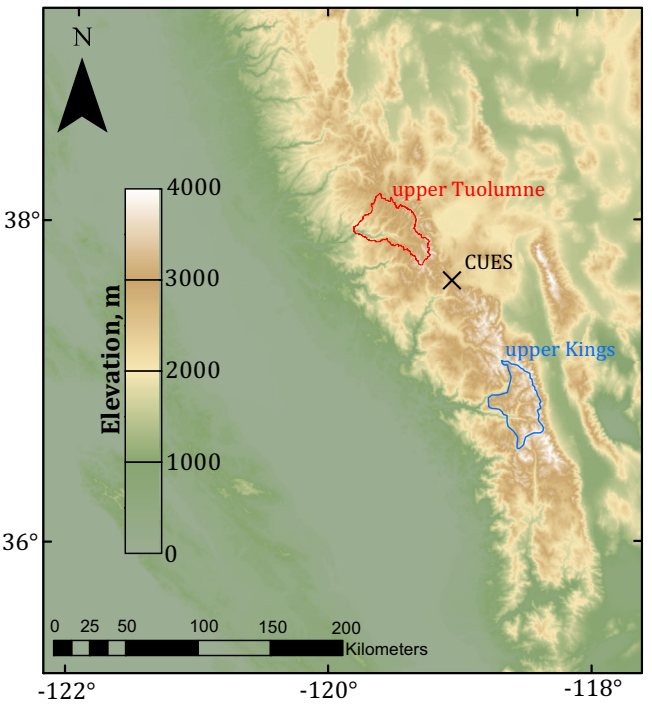

Figure 1. Elevation of the central and southern Sierra Nevada, with the upper Tuolumne River Basin, upper Kings River Basin, and CUES labeled.

inherently less accurate than f_{SCA} at 30 m from Landsat [*Rittger et al.*, 2013]. Attempts have been made to harness the strengths of both MODIS and Landsat with significant improvements in accuracy with inclusion of the daily MODIS f_{SCA} [*Durand et al.*, 2008]. Also, with MODIS measurements, snow cover on cloudy days can be interpolated [*Dozier et al.*, 2008] and date of melt-out can be determined more precisely, thereby reducing a source of error in reconstructed SWE [*Slater et al.*, 2013].

2.3. Snow Temperature

The snowpack's loss of energy through longwave emission depends on its surface temperature. Simple approximations for the snow surface temperature are often used [*Cline et al.*, 1998; *Jepsen et al.*, 2012; *Guan et al.*, 2013; *Girotto et al.*, 2014]. For example, *Molotch* [2009] assumes that the snow surface temperature equals the average daily air temperature but constrained to be no greater than 0°C. This questionable assumption leads to incorrect calculations of outgoing longwave radiation and imputing melt when the snow is frozen. Analysis of the hourly air and snow surface temperatures at the Senator Beck Study Plot from 2005 through 2014 [*Landry et al.*, 2014] (data available at http://www.snowstudies.org/data/] for the months of April through June with snow depth $\geq$0.30 m shows the snow temperature by *Molotch's* [2009] method to be too warm by an average of +3.9°C, with an average emitted longwave radiation error of +17 W m^{-2}. On the other hand, *Raleigh et al.* [2013a] recommend using the dew point temperature as the approximation for snow surface temperature. Comparisons with the same data set show that their method yields snow temperatures that are too cold by an average of −3.7°C, with an emitted longwave radiation error of −16 W m^{-2}. Our snowmelt model solves for the snow surface temperature as the equilibrium temperature that balances the energy exchanges, similarly to validated point energy balance models [*Outcalt et al.*, 1975; *Davis et al.*, 2001].

2.4. Validation

A goal for this study was to verify the SWE reconstruction in a location where spatially distributed SWE was estimated by ASO. Verification is a problem with all spatial snow models. Previous reconstruction models have been verified with point measurements [*Guan et al.*, 2013; *Rittger et al.*, 2016], or interpolated spatially using regression trees [*Cline et al.*, 1998; *Molotch and Margulis*, 2008; *Molotch*, 2009; *Girotto et al.*, 2014]. Verification using point measurements suffers from scale issues, exacerbated by complex terrain because snow courses and pillows located on flat ground may not represent snow on the surrounding terrain [*Dozier et al.*, 2016]. Likewise, regression tree estimates of SWE, which use point data as input, explain only 50% of the variance in snow accumulation [*Molotch and Bales*, 2005].

3. Study Areas

3.1. Upper Tuolumne River Basin

The upper Tuolumne River Basin (labeled in Figure 1) is a 1182 km^2 basin in Yosemite National Park, California. Elevations range from 1134 m to the summit of Mt. Lyell at 3997 m. Land cover ranges from shrubs and coniferous forest at the lower elevations to large areas of bare rock at the higher elevations [*Homer et al.*,

2015]. Runoff, primarily from snowmelt, feeds the Hetch Hetchy Reservoir, which provides municipal water and hydropower for 2.4 million people [*Bay Area Water Supply and Conservation Agency*, 2015]. We chose the upper Tuolumne River Basin for the SWE reconstructions because it was the first basin flown by ASO, in 2013, and it has the longest record of ASO measurements.

3.2. Upper Kings River Basin

The snowmelt-dominated upper Kings River Basin (also labeled in Figure 1), with area 1097 km^2, lies in the southern Sierra Nevada. Elevations range from 1552 to 4343 m at the summit of North Palisade. Like the upper Tuolumne, the basin land cover also ranges from shrubs and coniferous forest at the lower elevations to large areas of bare rock at the higher elevations [*Homer et al*., 2015]. This basin feeds the Kings River, a source of hydropower and agricultural water that serves 750,000 people in California's Central Valley and generates $3 billion in agriculture revenues [*Kings River Conservation District*, 2009]. We chose the upper Kings River Basin because an ASO flight coincided with acquisition of WorldView-3 imagery on 31 May 2015, thereby providing data to validate ASO's ability to identify snow. We note that on this date, SWE was at record low levels throughout the Sierra Nevada, so snow persisted only in the highest elevations, almost all above the tree line.

3.3. The CRREL/UCSB Energy Site (CUES)

The CRREL UCSB Energy Site (CUES in Figure 1) is located 23 km southeast of the most southern and highest point in the upper Tuolumne basin. At 2940 m in elevation, CUES represents the higher elevations of the upper Tuolumne basin. CUES was chosen because of its proximity to the upper Tuolumne and its extensive suite of quality-controlled and calibrated measurements at a temporal resolution of one minute [*Bair et al*., 2015] (data available at http://www.snow.ucsb.edu/). Since the 2013–2015 ASO measurements show almost no snow below 2000 m, we also examined other weather stations in the upper Tuolumne above 2000 m. These data are available from the California Data Exchange Center (http://cdec.water.ca.gov/); database identifiers and elevations are given in parentheses: Tuolumne Meadows (TUM, 2631 m); Dana Meadows (DAN, 2987 m); Paradise Meadow (PDS, 2332 m); Horse Meadow (HRS, 2560 m); and Slide Canyon (SLI, 2804 m). Of these stations, only TUM and DAN had continuous measurements of incoming shortwave radiation since the first ASO flight on 13 April 2013. However, these measurements do not distinguish between direct and diffuse radiation, which are needed to calculate solar irradiance on slopes, and they are aggregated over an hour (as averages, minima, or maxima) and thus not directly comparable to the instantaneous estimates from the National Land Data Assimilation System 2 (NLDAS-2) [*Cosgrove et al*., 2003; *Xia et al*., 2012], which we use for downscaling. Also, none of these stations provide measurements of incoming longwave or reflected radiation. DAN provides net solar radiation, from which snow albedo could be computed (without a terrain correction), but the measurements include large negative or constant values for extended time periods. In addition, calibration and maintenance records for instruments at TUM and DAN are not accessible so their accuracies are not known. Likewise, TUM and DAN are located in wilderness areas that are not accessible by vehicles during the winter, so instrument failures are only fixed in the summer. At CUES, maintenance is performed year round, with a documented overhaul each fall. For these reasons, we use CUES alone for validation of our energy balance model.

4. Methods

The comparison operates on the premise that ASO provides the best estimate of spatially distributed SWE, to which independent estimates from SWE reconstruction, spatial interpolation from ground measurements, and SNODAS can be compared. We also verified inputs to the reconstruction models using several validation sources. For inputs to the reconstruction models, we tested several alternatives: (i) snow albedo using a remotely sensed grain size and two other age-based models; (ii) f_{SCA} using different adjustments to account for snow obscured by canopy cover; and (iii) downscaled NLDAS-2 forcings against measurements from an energy balance site. Optimal inputs were then selected and used in two different reconstruction models, a full energy balance and a net radiation plus degree-day model. Additionally, we compared measurements of derived f_{SCA} from ASO to those independently measured from a WorldView-3 scene.

4.1. Reconstruction

At time j, the energy to melt snow, in W m^{-2}, is the product of the possible energy $M_{p,j}$ and the fractional snow cover $f_{SCA,j}$ [*Molotch and Bales*, 2005]:

$$M_j = f_{SCA,j} \times M_{p,j} \tag{1}$$

To estimate hourly (the model time step) SWE in mm at time j, M_j is summed during contiguous periods when $f_{SCA,j} > 0$.

$$SWE_j = m_f \sum_{0}^{N} M_{j|f_{SCA,j}>0} \tag{2}$$

with m_f as the melt factor

$$m_f = \frac{3600 \frac{\text{s}}{\text{h}} \times 1000 \frac{\text{mm}}{\text{m}}}{\lambda_f \rho_w} \approx 0.0108 \ \frac{\text{mm}}{\text{W m}^{-2} \text{ h}} \tag{3}$$

$\lambda_f = 3.34 \times 10^5$ J kg^{-1} is the enthalpy of fusion for water, and $\rho_w = 1000$ kg m^{-3} is the density of water. The maximum value of SWE is then the seasonal maximum accumulation. The constraint that $f_{SCA} > 0$ accounts for ephemeral snow, i.e., that appears and disappears. Reconstruction cannot provide SWE estimates earlier than the maximum, i.e., during the accumulation season. Theoretically, the peak SWE date can be estimated from the earliest date when $M_j \approx 0$ for an extended period of time. In practice, ancillary information on the date of peak SWE (such as from snow pillows) is used to define valid dates for reconstruction when such data are available [*Rittger*, 2012]. For this study, peak SWE dates for the basin come from basin-wide ASO SWE estimates.

We used f_{SCA} from the MODIS Snow-Covered Area and Grain Size algorithm (MODSCAG) [*Painter et al*., 2009] smoothed over time and space to eliminate noisy data and interpolate across cloudy days, in a way that places less weight on pixels further off nadir [*Dozier et al*., 2008]. Discrimination between snow and clouds uses a radiative transfer model [*Dozier*, 1989] and a persistence filter. The f_{SCA} was further adjusted for viewable gap fraction between trees using a static canopy cover adjustment [*Molotch and Margulis*, 2008; *Raleigh et al*., 2013b]:

$$f_{SCA} = \min\left(\frac{f_{SCA,\ raw}}{1-cc}, 1\right) \tag{4}$$

$f_{SCA,\ raw}$ is the smoothed fractional snow cover end-member from MODSCAG, and cc is the fractional canopy cover from the 2011 National Land Cover Database (NLCD) [*Homer et al*., 2015]. Values for f_{SCA} exceeding 1.0 were set to 1.0. Likewise, for pixels with $cc = 1$, equation (4) goes to infinity, so no adjustment was applied $\left(f_{SCA} = f_{SCA,\ raw}\right)$. A dynamic adjustment using the MODSCAG vegetation fraction (f_{veg}) was also tried, i.e., $1 - f_{veg}$ in the denominator of equation (4), but yielded higher bias than the static canopy adjustment (section 5.4), thus it was not used. For the f_{SCA} and all other spatial data in reconstruction, we projected the data at 500 m to the Albers equaconic projection centered on California (hereafter called the California Albers projection).

Calculation of potential melt is from energy balance components

$$M_{p,j} = R_j + H_j + L_j + G_j \tag{5}$$

where R is net radiation, H and L are sensible and latent heat exchanges, and G is heat flow in/out of the snowpack, all at time step j. We assume the snowpack is either melting or heat flow into the pack is small compared to the other fluxes, so $G \approx 0$. Moreover, melt is set to zero when the calculation would be negative. Thus, equation (5) becomes

$$M_p = \max(R + H + L, 0) \tag{6}$$

Other reconstruction models have used a degree-day coefficient to model turbulent fluxes [e.g., *Molotch*, 2009]. For comparison, we also implemented the SWE reconstruction model with a restricted degree-day approach [*Kustas et al*., 1994; *Brubaker et al*., 1996]:

$$(H+L)_{dd} = \frac{a_r}{m_f} \max(0^\circ\text{C}, T_a) \tag{7}$$

T_a is the air temperature above 0°C and $a_r = 0.14$ mm d^{-1} K^{-1} is an empirical melt factor relating air temperature to the convective contributions to melt, calculated using 2013–2015 March–May averages at CUES

[*Brubaker et al.*, 1996, equation A10]. Thus, $a_r/m_f = 0.54$ W m^{-2} K^{-1} d^{-1}. This a_r value is significantly lower than values in other studies [e.g. 0.90–2.00 mm day^{-1} K^{-1}, *Brubaker et al.*, 1996; *Molotch and Bales*, 2006]. For this degree-day version of the model, the snow surface temperature T_s is set the as the lesser of 0°*C* or T_a, following *Molotch and Margulis* [2008]. Note that the treatment of the turbulent fluxes and the solution for surface temperature are the only differences between the full energy balance, EB, equation (6), and the restricted degree-day, DD, equation (7), reconstruction models. In both models, using either equation (6) or (7), melt does not occur when $T_s < 0$ °*C*.

Net radiation *R* is expressed as

$$R = S_{\downarrow}(1-\alpha) + I_{\downarrow} + I_{\uparrow} \tag{8}$$

$S_{\downarrow}$ is incoming solar radiation, α is the broadband snow albedo, $I_{\downarrow}$ is incoming longwave radiation, and $I_{\uparrow}$ is outgoing longwave radiation. The energy balance model is sensitive to snow albedo. The broadband albedo α is computed from the smoothed remotely sensed grain radius from MODSCAG and the local solar zenith angle [*Gardner and Sharp*, 2010]. These albedo estimates were further reduced by half the smoothed Δ_{vis} term from the MODIS Dust and Radiative Forcing in Snow [MODDRFS, *Painter et al.*, 2012] to account for light absorbing impurities,

$$\alpha = \alpha_{clean} - \Delta_{vis}/2 \tag{9}$$

α_{clean} is the modeled clean snow albedo and Δ_{vis} is an estimate of the difference between the dirty and the clean snow albedo in the visible spectrum (0.350–0.876 μm), where light absorbing impurities in snow decrease the spectral reflectance. Since α is a broadband albedo and about half the sun's energy is in the visible spectrum [*Gueymard*, 2004], we use half the Δ_{vis} estimate.

For comparison, we also compute net radiation with two other snow albedo models: the Biosphere-Atmosphere Transfer Scheme (BATS) [*Dickinson et al.*, 1993; *Liang et al.*, 1994] and a simple aging model based on the time since the last snowfall [*Walter et al.*, 2005]. Both albedo models require estimates of when the last snowfall occurred, which we obtained from Mammoth Mountain Ski Patrol daily weather observations, using the threshold of 10 mm of new SWE to reset the snow albedo [*Dickinson et al.*, 1993]. The simple model based on aging requires a new snow albedo, which we set at 0.86, based on the CUES measurements. The BATS model requires the snow surface temperature T_s, the lesser of 0°*C* or T_a, and the cosine of the solar zenith angle (section A1).

All energy balance terms, with the exception of those used to calculate a_r, are modeled using downscaled forcings from the 1/8° NLDAS data. The downscaling process involves a bicubic resampling of the 1/8° forcings and elevation model to the model scale. In this study, the model scale is 500 m, the size of a MODIS pixel in the "land" spectral bands 1 through 7. For terms that depend on elevation, we used the difference between the DEM from the Shuttle Radar Topography Mission [*Farr et al.*, 2007] and the NLDAS DEM, both resampled to 500 m resolution. Canopy data came from the National Land Cover Dataset resampled using Gaussian pyramid reduction [*Burt and Adelson*, 1983] (implemented in MATLAB as impyramid) to 500 m.

4.2. Interpolation From Snow Pillows

For comparison to the reconstructed SWE measurements, we interpolated the SWE values from snow pillows and courses in three dimensions [*Okabe et al.*, 2000] (implemented in MATLAB as scatteredInterpolant), constrained by snow-covered area. Daily SWE values from 119 snow pillows and 249 snow courses from 2013 to 2015 were downloaded from the California Data Exchange Center and manually cleaned for errors, such as spikes and spurious summer values. A 3-D convex hull (*x*, *y*, elevation) was created for each day using f_{SCA} at 500 m resolution from the same smoothed time-space f_{SCA} cubes used for reconstruction. Outside the hull, $f_{SCA} = 0$. Then, for each day, a 3-D bilinear interpolation of SWE was applied to the volume enclosed by the hull, using the SWE values from snow pillows and snow courses. SWE from snow pillows are available daily, but each snow course is only sampled a few times a year; thus, the interpolation relies more on pillow measurements. For elevations within the hull, but above/below the highest/lowest

elevations covered by the pillows and courses, SWE was extrapolated using nearest neighbors. Finally, these raw SWE values $SWE_{interp,raw}$ were multiplied by f_{SCA} to account for each pixel's varying snow cover:

$$SWE_{interp} = SWE_{interp,raw} \times f_{SCA} \quad (10)$$

4.3. Snow Data Assimilation System (SNODAS)

For another model comparison, we included SWE from SNODAS [*Barrett*, 2003], NOAA's modeling and data assimilation system from the National Operational Hydrologic Remote Sensing Center. SNODAS ingests and downscales daily output from numerical weather models, an energy-balance and mass balance snow model, and airborne and ground-based snow measurements. Each day, analysts choose whether to use modeled or observed snow measurements. SNODAS daily estimates were downloaded from the National Snow and Ice Data Center [*NSIDC*, 2016]. The SNODAS spatial grid covers the US and parts of southern Canada in a geographic projection at 30 arc sec. The SNODAS SWE data were reprojected to the 500 m target resolution in the California Albers projection.

4.4. Validation Data

4.4.1. Data From the Airborne Snow Observatory

Snow depth at 3 m resolution and SWE at 50 m resolution in a Universal Transverse Mercator projection were obtained from ASO for the upper Tuolumne River Basin over the 2013–2015 water years, comprising 27 dates. Snow depths at 3 m resolution were also obtained for the upper Kings River Basin for 31 May 2015. Accuracy assessments using point measurements show a depth uncertainty of 8 cm at 3 m spatial resolution, average depth uncertainty of less than 0.5 cm at 50 m resolution, and 1–10 cm of uncertainty for SWE at 50 m resolution, depending on absolute SWE [*Painter et al.*, 2016].

The 3 m ASO snow depth was converted to a binary mask (1 for snow depth >0; 0 otherwise). This mask overestimates snow-covered area slightly, as mixed 3 m pixels with snow are assumed to be 100% snow covered. The mask was then upscaled, and reprojected to a California Albers projection to match the f_{SCA}. The upscaling occurred in multiple steps using Gaussian pyramid reduction. The final step to the 500 m target resolution used bilinear interpolation [*Glassner*, 1993] (implemented in MATLAB as imresize), yielding ASO-derived f_{SCA} at 500 m. Snow depth and albedo were also upscaled to the California Albers projection.

4.4.2. Energy Balance Forcings

Modeled energy balance forcings were compared with measurements from CUES during the 2013–2015 water years, except for snow albedo where measurements from 2016 at CUES were used. These included direct and diffuse shortwave radiation, wind speed, incoming longwave, and air temperature. Modeled values were only corrected for elevation, not for terrain or canopy cover, to match the values recorded by the level, unobstructed instruments at CUES. CUES does not have thermal infrared thermometers for measuring snow surface temperature.

Ideally, measurements from 2013 to 2015 would have been used for snow albedo. However, given the shallow snow depths for 2013–2015, measurements from the downlooking radiometers at CUES, which are installed 6 m above the ground, were unreliable for measuring snow albedo during that period. Essentially, snow albedo measurements were too low because the downlooking radiometers' field of view contains trees and other dark objects when snow depths are low. In September 2015, we installed an adjustable downlooking radiometer boom to remedy this problem. There are now limited ($N = 116$) but reliable daily measurements of ground-based snow albedo at CUES, with the caveat that these albedo measurements only cover the 2016 water year. Because of frequent storms in December, we only compared measurements from January through May 2016. These albedo measurements were corrected for slope and aspect of the snow surface using an automated scanning terrestrial lidar [*Bair et al.*, 2015] (describe these corrections). ASO offers broadband snow albedo estimates, but these are not reliable because the ASO Itres CASI-1500 spectrometer only covers a spectral range from 0.365 to 1.050 μm. To model broadband snow albedo using this spectrometer, the rest of the shortwave infrared solar spectrum, where most of the absorption depends on grain size, must be extrapolated.

4.4.3. WorldView Imagery

To validate ASO's ability to identify snow, we compared WorldView-3 imagery to the 3 m snow mask created from the ASO snow depth. The WorldView images were acquired on 31 May 2015 over the upper Kings

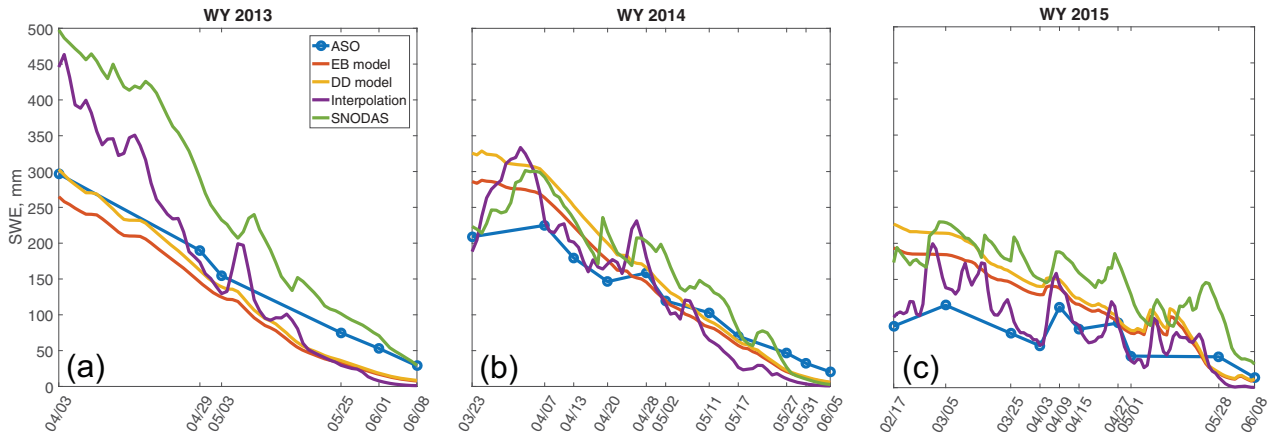

Figure 2. Basin average ASO SWE compared to full energy balance (EB) reconstruction; net radiation/degree-day (DD) reconstruction; snow pillow interpolation (Interpolation), and the Snow Data Assimilation System (SNODAS) for the upper Tuolumne for (a) 2013, (b) 2014, and (c) 2015.

River Basin and coincided with an ASO flight. Uncalibrated red-green-blue (RGB) WorldView imagery was upscaled from 0.3 to 3 m resolution to match the snow mask. The RGB imagery was then classified using *k*-means clustering [*Hastie et al.*, 2009] (implemented in MATLAB as kmeans), with five classes. The resulting snow classifications were checked manually for accuracy by comparison with the visible imagery. The WorldView scenes were acquired near midday, with solar zenith angles ~20°, so few areas were shadowed. The uncertainty for pixel location (RMSE = 3.9 m, provided as metadata with the WorldView imagery) is significantly greater than the image resolution. The uncertainty in location for the ASO snow depth at 3 m resolution is about 1.5 m [*Painter et al.*, 2016]. To account for these uncertainties, a best of 3 × 3 pixel neighborhood (9 m^2) was used for the comparison.

5. Comparisons and Discussion

5.1. Snow Water Equivalent

Figure 2 compares the ASO SWE, averaged over the upper Tuolumne River Basin in years 2013 through 2015, to four methods of estimating the same variable that can apply over whole mountain ranges: reconstruction using energy balance and degree-day methods to calculate snowmelt, spatial interpolation from snow pillows, and SNODAS (the Snow Data Assimilation System). Table 1 shows the error statistics: *bias* and mean absolute error (*MAE*), as described in Appendix B.

5.1.1. Reconstructed Snow Water Equivalent

Since reconstruction only provides valid SWE estimates back to the last peak SWE date, we computed error statistics only back to the peak SWE date for the basin, obtained from ASO measurements. The first ASO measurement date occurred before the peak in 2014 and 2015 but may have been after the peak SWE in 2013, thus error statistics were computed starting at the first ASO measurement date in 2013. Also, ASO measurements showed two peak SWE values for the basin in 2015, 112 mm on 9 April 2015 and 114 mm on 5 March 2015; error statistics were only computed back to the later peak, on 9 April 2015.

The EB and DD versions of reconstruction had similar *MAE* values for all years, 26% and 28%, respectively (Figures 2a–2c and Table 1), ranging from 20 to 31% for the EB model and 18 to 38% for the DD model. The EB model had a 0% bias on average, with a range from −11% to +10%, whereas the DD model had a 5% bias on average, ranging from −7% to +14%. Analysis of the energy balance components for both models shows large differences in longwave radiation emitted from the snowpack ($I_{\uparrow,\mathrm{eb}}$ and $I_{\uparrow,\mathrm{dd}}$ in Figures 3a–3c) with small differences in the net turbulent transfer terms ($H+L$ in Figures 3a–3c). Since emitted longwave radiation is proportional to T_s^4, the differences in both terms can be explained by colder snow surface temperatures in the EB model. All else being equal, less emitted longwave radiation would cause more melt, but the colder T_s reduces melt by limiting the times when the snowpack is at 0°*C*.

Table 1. Errors for Each Method at Peak SWE and For All Dates After, With ASO Considered the Standard[a]

	Method	Bias (mm)	Bias (%)	Mean Absolute Error (mm)	Mean Absolute Error (%)
2013	ASO	0	0	0	0
	EB model	−34	−11	34	26
	DD model	−22	−7	24	18
	Interpolation	−2	−1	52	39
	SNODAS	71	24	71	53
2014	ASO	0	0	0	0
	EB model	+1	0	22	20
	DD model	+15	+7	30	27
	Interpolation	−10	−4	24	22
	SNODAS	+29	+13	40	36
2015	ASO	0	0	0	0
	EB model	+11	+10	20	31
	DD model	+16	+14	24	38
	Interpolation	−2	−2	14	22
	SNODAS	+68	+61	68	107
Averages	ASO	0	0	0	0
	EB model	−7	0	25	26
	DD model	+3	+5	26	28
	Interpolation	−5	−2	30	28
	SNODAS	+56	+33	60	65

[a]The percent errors are calculated relative to the mean ASO mean values for the same dates.

It is possible that the EB model T_s is too cold at night, since there is no conduction between snowpack layers built into the model. Conversely, the T_s from the DD model is likely too warm. As noted, we do not have snowpack surface temperatures at CUES for comparison. Inversion of $I_{\uparrow,eb}$ and $I_{\uparrow,dd}$ using the Stefan-Boltzmann equation over the time periods shown in Figure 3a gives a T_s of −12.5°C for the EB model and −0.8°C for the DD model.

The slightly lower SWE values for the EB model also resulted from a negative net turbulent transfer $(H+L)$, whereas equation (7) constrains $H+L$ in the DD model to be nonnegative. The effect on melt is small but not negligible. For instance, the mean $(H+L)_{eb}$ and $(H+L)_{dd}$ values (Figure 3a) are −4 W m^{-2} and +2 W m^{-2}, affecting melt values by −1.0 and +0.5 mm/d.

The EB and DD reconstruction models compare favorably with other reconstruction models using MODIS f_{SCA}. *Guan et al.* [2013] report −40% bias and an MAE of 47% for a reconstruction model driven with MODSCAG f_{SCA} (but smoothed differently) and validated using manual snow surveys in California's Sierra Nevada. *Molotch and Margulis* [2008] report an MAE of 50% for a reconstruction model run in Colorado using f_{SCA} from the NASA MOD10A1 product [*Hall et al.*, 2006] and validated with field campaigns. The same simulation was then run with MODSCAG f_{SCA}, resulting in a lower MAE (24%), highlighting the model's sensitivity to f_{SCA} [*Molotch et al.*, 2010].

Our reconstruction models also compare favorably with reconstruction models run with finer resolution f_{SCA} from Landsat, which offers improvements in accuracy at the expense of coarse 16 day temporal resolution. *Molotch and Margulis* [2008] report an MAE of 23% using a reconstruction model driven with f_{SCA} from Landsat and verified with SWE modeled by regression trees. *Girotto et al.* [2014] report a bias of 7%, verified with

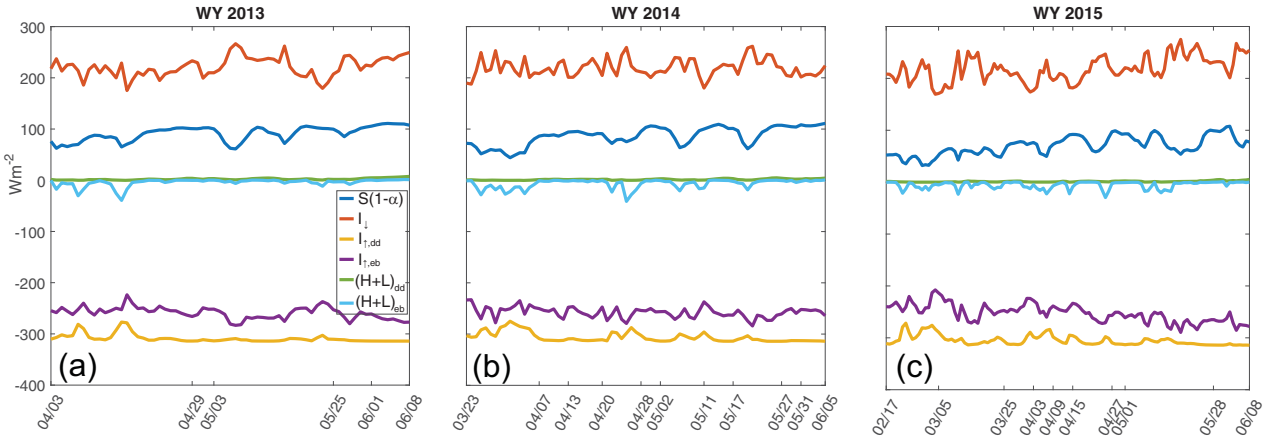

Figure 3. Daily averages for energy balance components over snow-covered areas in the upper Tuolumne for (a) 2013, (b) 2014, and (c) 2015. The curves are net solar, $S_{\downarrow}(1-\alpha)$; incoming longwave, $I_{\downarrow}$; longwave emitted from the snowpack from the EB and DD models, $I_{\uparrow,eb}$ & $I_{\uparrow,dd}$; and net turbulent transfer terms from the EB and DD models, $(H+L)_{eb}$ & $(H+L)_{dd}$.

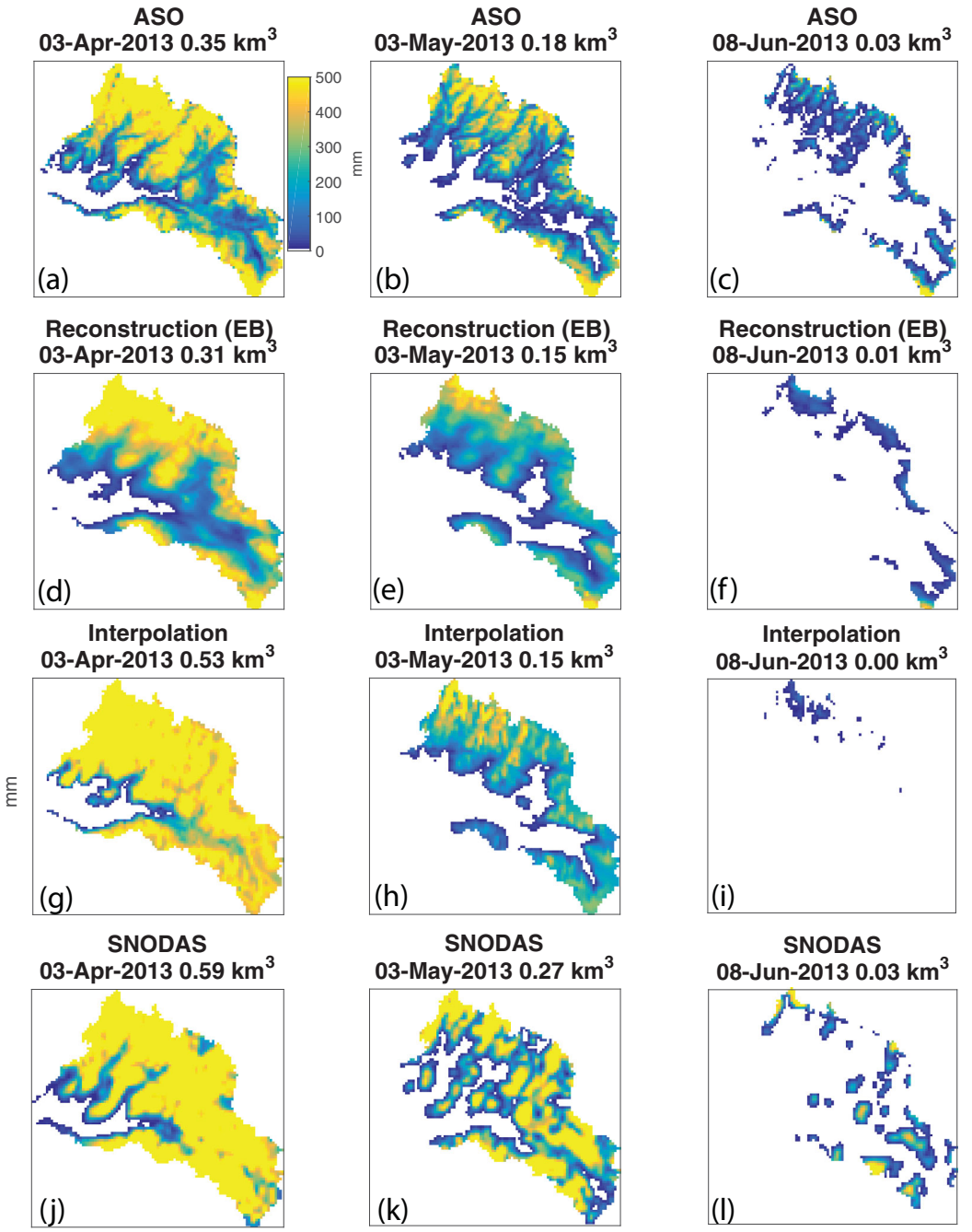

Figure 4. ASO SWE for the upper Tuolumne River Basin compared with reconstruction (EB), snow pillow interpolation, and SNODAS for (a, d, g, j) 3 April 2013; (b, e, h, k) 3 May 2013; and (c, f, i, l) 8 June 2013. Images show SWE, in millimeters, at 500 m resolution, the reconstruction model resolution.

field campaigns in the Tokopah Basin in the Sierra Nevada, although the verification data comprised modeled SWE from regression trees, which have their own errors.

5.1.2. Spatial Interpolation From Snow Pillows and Courses

The EB model narrowly outperformed interpolation from snow pillows. For the 2013–2015 mean, snow pillow interpolation had a bias and *MAE* of −2% and 28%, ranging from −1% to −4% and 22% to 39%. Since the reconstruction models and snow pillow interpolation used the same f_{SCA} inputs, which were shown to be very accurate using the ASO-derived f_{SCA} for validation (section 5.4), our findings show that f_{SCA} is critically important for accurate results from both models.

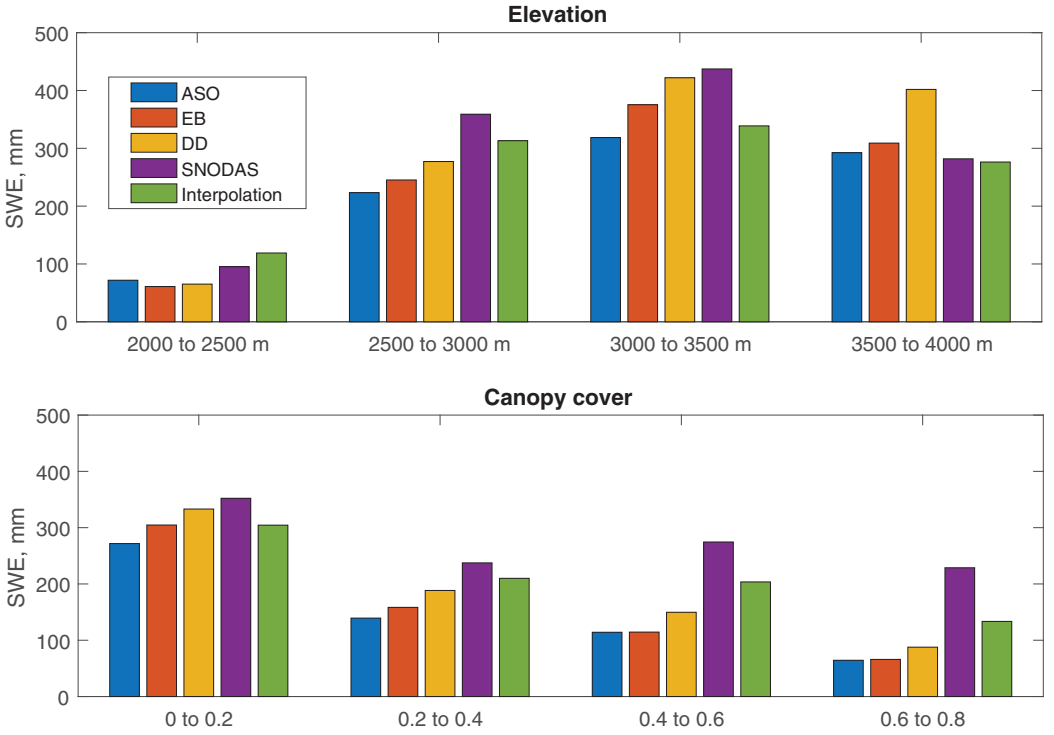

Figure 5. SWE binned by (a) elevation and (b) canopy cover for all methods for mean peak SWE values for 2013–2015.

5.1.3. SNODAS, the Snow Data Assimilation System

Both reconstruction models vastly outperformed SNODAS, which overpredicted SWE in every year, with a mean bias of +33% and MAE of 65%, and annual biases ranging from +13% to +61% and *MAE* values from 36% to 107%.

It is unclear why SNODAS overestimated SWE in every year. Other comparisons show problematic results from SNODAS, both underestimates and overestimates [*Dozier*, 2011; *Rittger*, 2012; *Dozier et al*., 2016]. No peer-reviewed publications explain the details of the SNODAS model structure, so it is difficult to trace the source of errors, either in the calculations of orographic enhancement to precipitation or in the choice of surface observations to assimilate. The model resolution for SNODAS is 30 arc sec, about 1 km, which is 2× that of the reconstruction and snow pillow interpolation models, but this coarser resolution is an unlikely cause of the high bias and *MAE*. Because SNODAS assimilates many publicly available snow measurements, validation studies from independent observations for comparison have been scarce. *Clow et al*. [2012] report an RMSE of 120 mm (48% of mean) for sites in Colorado and suggest that SNODAS could be substantially improved by accounting for wind-redistributed snow.

Table 2. SWE Bias (Using ASO for Verification) for Each Method at Mean Peak SWE From 2013 to 2015

Bias by Elevation (mm)	2000–2500 m	2500–3000 m	3000–3500 m	3500–4000 m
EB	−11 (−15%)	22 (10%)	57 (18%)	17 (6%)
DD	−7 (−9%)	54 (24%)	103 (32%)	109 (37%)
SNODAS	23 (33%)	136 (61%)	119 (37%)	−11 (−4%)
Interpolation	47 (66%)	90 (40%)	20 (6%)	−16 (−6%)
Bias by Canopy Cover (mm)	**0–0.2**	**0.2–0.4**	**0.4–0.6**	**0.6–0.8**
EB	33 (12%)	19 (14%)	0 (0%)	2 (2%)
DD	61 (23%)	49 (35%)	36 (31%)	23 (36%)
SNODAS	80 (30%)	98 (70%)	160 (140%)	164 (255%)
Interpolation	33 (12%)	71 (51%)	89 (78%)	69 (107%)

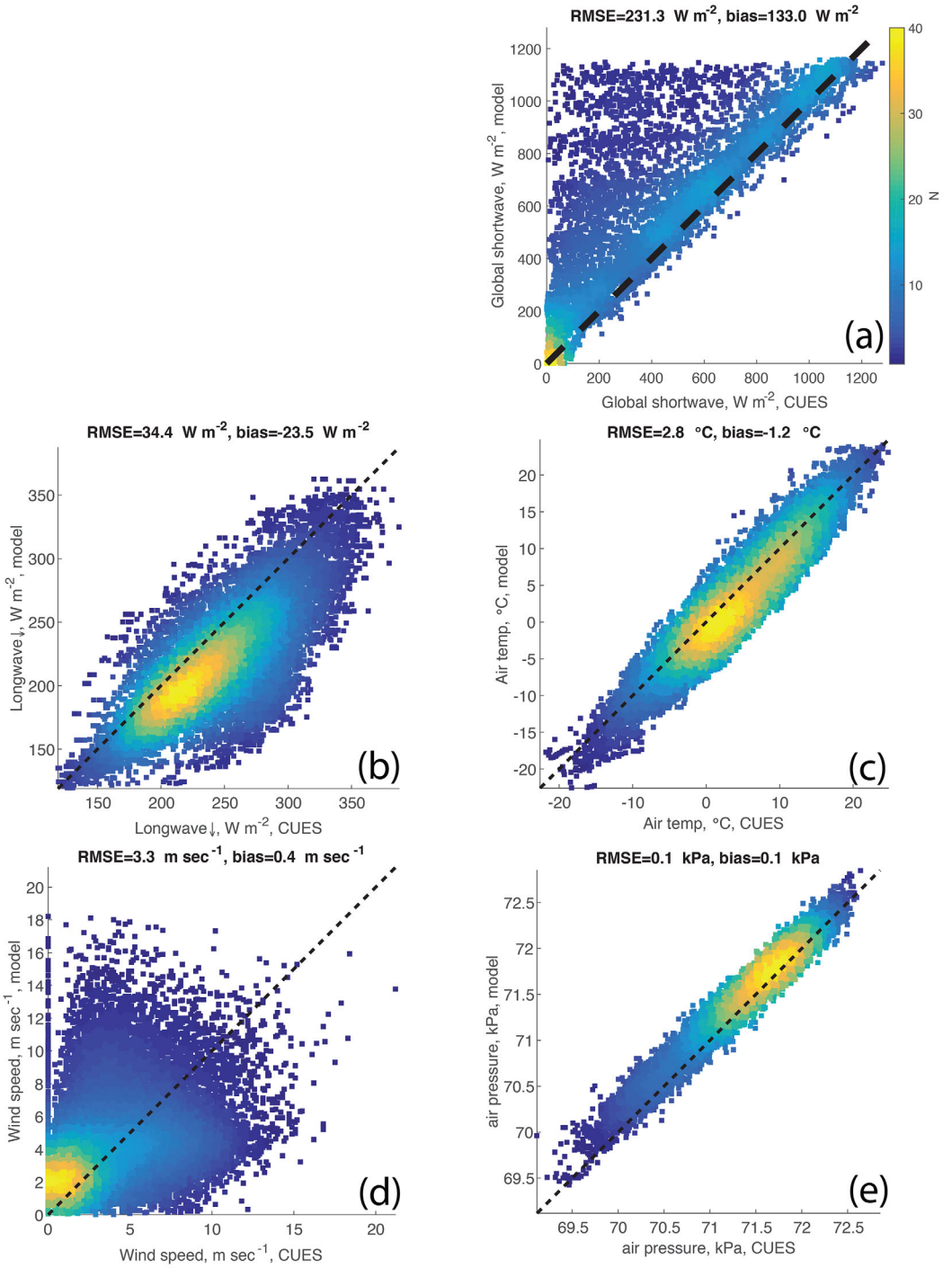

Figure 6. Modeled versus measured density scatter plots of hourly: (a) global shortwave; (b) incoming longwave; (c) air temperature; (d) wind speed; and (e) air pressure. All measurements made at the CRREL UCSB Energy Site (CUES) on Mammoth Mountain during the 2013–2015 water years. Shortwave values at night are excluded. The colors scale linearly with the number of measurements *N*. The model results are for the 500 m pixel containing CUES.

5.2. Spatial Variability

Visual examination of the spatial distribution of SWE from the EB model and ASO for three dates in the 2013 melt season (Figures 4a–4f) shows that the EB model reproduced the spatial SWE patterns well. Some of the finer spatial patterns (Figure 4b compared to Figure 4e) are lost and some of the late season SWE is

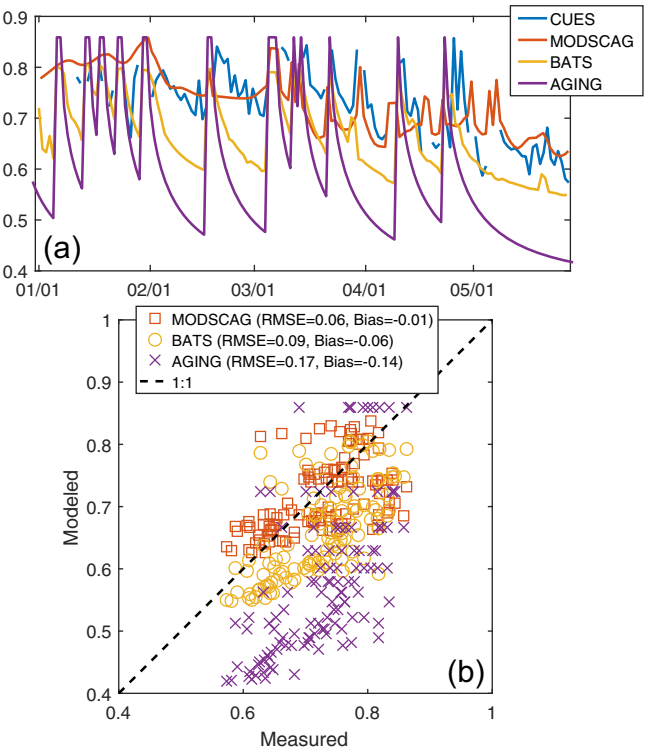

Figure 7. (a) Time series and (b) 1:1 comparison of snow albedos from three different models versus measured albedo at CUES during January through May 2016.

not detected (Figure 4c compared to Figure 4f), probably because of the 0.10 f_{SCA} detection limit set for MODSCAG [*Painter et al.*, 2009]. Visual comparison of the spatial distribution of SWE for the same dates for snow pillow interpolation and SNODAS (Figures 4g–4l) shows more SWE throughout the basin for the first date (Figures 4g and 4j) and a failure to identify the one area with perennial snow, the Lyell glacier at the southern end of the basin (Figures 4h, 4i, 4k, and 4l). The EB model identifies this area as covered by snow throughout the melt season (Figures 4e and 4f).

Figures 5a and 5b and Table 2 compare SWE binned by elevation and canopy cover, at the dates of mean peak SWE. The EB model has lower SWE bias in three of four elevation bins and all of the canopy cover bins when compared to the DD model. The EB model SWE bias ranges from −15% to +18% for the elevation bins and 0 to 12% for the canopy cover bins, with almost no bias for the 0.4–0.6 and 0.6–0.8 bins. The DD model SWE bias for elevation ranges from −9% to +32% with the largest error at the highest elevations (3500–4000 m). In comparison, the SWE bias for the EB model was only +6% for the 3500–4000 m bin. For canopy cover, the DD model SWE bias ranged from +23% to +36%. SNODAS and snow pillow interpolation showed much larger biases than either reconstruction model. The SWE bias by elevation for SNODAS ranged from −4% to +61%. For canopy cover, the SWE bias for SNODAS ranged from +30% to +255%, with the biggest value (at 0.6–0.8 canopy cover fraction) representing the worst bias of any model. For interpolation, the SWE bias by elevation ranged from −6% to +66%; the SWE bias by canopy cover ranged from +12% to +107%.

SWE results were also binned by slope and aspect, but these analyses did not provide insightful results, with different bins showing little variation. We hypothesize that the complex terrain of the upper Tuolumne basin flattens slopes when upscaled to the 500 m model resolution. At 500 m resolution, 5% of pixels have slopes greater than 25° and 0.6% have slopes greater than 35°, whereas at 50 m resolution, 31% of pixels have slopes greater than 25° and 12% have slopes greater than 35°. Thus, SWE comparisons with slope and aspect at the 500 m model resolution result in misleading interpretations. For instance, ASO measurements upscaled to 500 m show slightly more SWE on south-facing slopes than on those that face north. At 50 m resolution, the opposite is true, and visual observations usually show more snow on north-facing slopes.

5.3. Energy Balance Components

Figure 6 compares values of the components of the surface energy balance derived from NLDAS-2 with measurements at CUES (described in sections 3.3 and 4.4.2).

5.3.1. Incoming Solar Radiation

Incoming solar radiation from NLDAS was a major source of error. The modeled RMSE and bias were 231 W m^{-2} and +133 W m^{-2}, respectively (Figure 6a). It appears that the high bias resulted when NLDAS-2 misidentified cloudy periods as cloud free, as *Hinkelman et al.* [2015] also identify (we filter CUES radiation measurements to remove values when the uplooking radiometers are covered by snow, so this is not the source of the overestimates). Combining equation (3) with a broadband snow albedo of 0.75, the bias equates to an overestimated potential melt of 8.6 mm/d. We note that for this error analysis, unlike in other

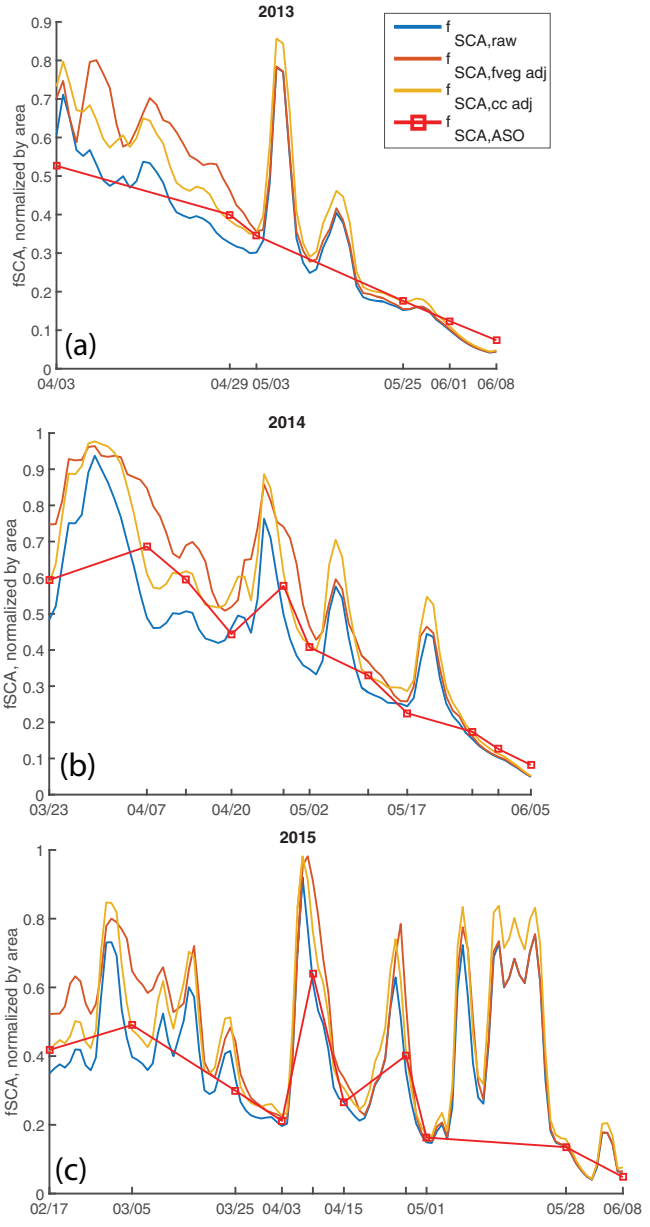

Figure 8. Time-space smoothed f_{SCA} compared to ASO-derived f_{SCA} for water years: (a) 2013, (b) 2014, and (c) 2015. The three curves show three corrections: uncorrected ($f_{SCA,raw}$); corrected by vegetation fraction ($f_{SCA,fveg\ adj}$); corrected by static canopy cover ($f_{SCA,cc\ adj}$) which was chosen for the reconstructions because of its low bias and MAE. Model resolution is 500 m.

reconstruction studies [e.g., *Jepsen et al.*, 2012; *Rittger et al.*, 2016], we exclude values of zero at night, given that these are easy to model. Also, we compare hourly rather than daily values. Both factors increase the apparent sizes of errors. For instance, inclusion of the zero values at night using modeled and measured daily values reduces the RMSE and bias to 77 W m^{-2} and +57 W m^{-2}. These values are within ranges reported by *Rittger et al.* [2016], who examined daily average errors for downscaled NLDAS-2 shortwave radiation across the Sierra Nevada using the same downscaling techniques and report RMSE values ranging from 32 to 79 W m^{-2} and bias ranging from −41 to +65 W m^{-2}. CUES is a difficult place to accurately downscale 1/8° NLDAS-2 radiation. The site is often cloudy while areas only a few kilometers to the east are clear. On the other hand, the site represents much of the snow-covered region of the Central Sierra Nevada.

5.3.2. Incoming Longwave Radiation

The modeled incoming hourly longwave values (Figure 6b) have an RMSE of 34 W m^{-2} and a bias of −24 W m^{-2}. Again, the negative bias is likely related to cloud issues. Clouds increase incoming longwave radiation. When NLDAS fails to identify clouds when they are present, one would expect a negative bias in the incoming longwave radiation and a positive bias in the solar radiation. The longwave bias equates to −6.0 mm/d underestimate of potential melt. These RMSE values compare with those measured by *Rittger et al.* [2016], who report RMSE and bias values of 38 W m^{-2} and −30 W m^{-2}, respectively, for two Sierra Nevada stations.

5.3.3. Air Temperature

The modeled hourly air temperatures (Figure 6c) have an RMSE of 2.8°C and a bias of −1.2°C. For the DD model, this bias can be converted to melt by multiplying by a_r in equation (7). Doing so shows a bias in melt of −0.17 mm/d. These values fall within the error ranges reported by *Rittger et al.* [2016], who show RMSE values of 1.3–3.7°C and biases of −2.4 to +2.3°C.

5.3.4. Wind Speed

The modeled hourly wind speeds (Figure 6d) have an RMSE of 3.3 m s^{-1} and a bias of +0.4 m s^{-1}. The RMSE and bias are higher than previous studies that used the same wind model forced with point observations. *Liston and Elder* [2006] and *Musselman et al.* [2015] report RMSE less than 1.5 m s^{-1} and bias less than +0.3 m s^{-1}, again pointing to errors in the NLDAS data as the source of inaccuracies. Wind speed is used in calculating the

Table 3. Error Table for f_{SCA} at 500 m Resolution, Adjusted Using Different Methods (Section 4.1) Validated With ASO-Derived f_{SCA}

	Method	Bias (%)	Mean Absolute Error (%)
2013	f_{SCA}, raw	−15	20
	f_{SCA}, f_{veg} adj	−3	20
	f_{SCA}, cc adj	−2	16
2014	f_{SCA}, raw	−15	17
	f_{SCA}, f_{veg} adj	8	19
	f_{SCA}, cc adj	0	12
2015	f_{SCA}, raw	−2	12
	f_{SCA}, f_{veg} adj	25	26
	f_{SCA}, cc adj	16	16
Mean	f_{SCA}, raw	−11	16
	f_{SCA}, f_{veg} adj	10	22
	f_{SCA}, cc adj	5	15

exchange coefficient $D_{h,\lambda}$ in equation (A20), which is used in the sensible and latent heat flux calculations. However, sensible and latent heat fluxes tend to be similar in magnitude and opposite in sign [*Marks and Dozier*, 1992]; thus, errors in sensible and latent heat flux caused by incorrect wind speed often cancel each other in the energy balance calculations.

5.3.5. Air Pressure

Air pressures (Figure 6e) have an RMSE of 0.1 kPa and bias of +0.1 kPa, both very low, suggesting that the modeled temperature lapse rate of −6.5 K/km is a reasonable value to use in the hydrostatic equation to calculate the elevation dependence of air pressure.

5.4. Snow Albedo

Compared to our measurements at CUES, all albedo models underestimated, but the MODSCAG/MODDRFS remotely sensed albedo was the most accurate, with an RMSE of 0.06 and a bias of −0.01 (Figures 7a and 7b). In comparison, BATS had an RMSE of 0.09 with a bias of −0.06 and the simple aging model had an RMSE of 0.17 and a bias of −0.14. Given an average incoming shortwave radiation of 250 W m^{-2}, the MODSCAG/MODRFS bias of −0.01 would cause a 0.7 mm overestimate of potential melt per day, whereas the −0.06 bias from BATS would cause a 3.9 mm/d overestimate of potential melt and the −0.14 bias from the simple aging model would cause a 9.1 mm overestimate. We caution that our verification data set is limited (116 measurements) and does not include very dirty snow with low albedos. The lowest measured albedo at CUES in the verification data set is 0.57. Very dusty old snow can have albedos as low as 0.33, but while this magnitude of contamination is common in the mountains of the Colorado River Basin [*Painter et al.*, 2013], such contamination seldom occurs in the Sierra Nevada. Further verification of the MODSCAG/MODDRFS remotely sensed albedo is needed.

5.5. Vegetation Adjustments to Fractional Snow-Covered Area

Figures 8a–8c and Table 3 compare the ASO measurements of snow-covered area (f_{SCA}) to three adjustments to the MODSCAG f_{SCA} in equation (4) over the 3 year period, 2013–2015 water years. The mean biases are −11% for unadjusted MODSCAG, +10% for MODSCAG adjusted by f_{VEG}, and +5% for MODSCAG adjusted by static *cc*. The corresponding MAE values are 16%, 22%, and 15%. Because the static *cc* adjustment has the lowest combined bias and MAE, we chose it for the reconstructions. Other research has proposed that f_{SCA} at resolutions of more than a few meters requires an adjustment for viewable gap fraction of the canopy [*Raleigh et al.*, 2013b; *Rittger et al.*, 2013], thus it is not surprising that the unadjusted MODSCAG f_{SCA} had the highest bias. It is unclear why the dynamic MODSCAG f_{SCA} adjustment did not perform as well as the static adjustment. Perhaps shadows from trees caused a mapping error. Note that the spikes in the curves in Figures 8a–8c for the three different adjustments to MODSCAG f_{SCA} in between ASO flights resulted from storms during the melt season. ASO cannot fly during storms; therefore, these increases in f_{SCA} were not verified.

Table 4. Statistics for ASO/WorldView Snow Cover Comparison in the Kings River Basin for 31 May 2015 Using WorldView for Verification

N	88,469,081
Recall	0.992
Precision	0.990
Accuracy	0.998
F	0.991

5.6. Snow-Covered Area Derived by ASO and WorldView

Table 4, comparing scalar metrics of the snow-covered areas derived by ASO and WorldView-3 over a best of 3 × 3 neighborhood, shows excellent agreement with *Recall*, *Precision*, *Accuracy*, and *F* score all no less than 0.99 (definitions of these metrics are in Appendix B, equations B4–B7).

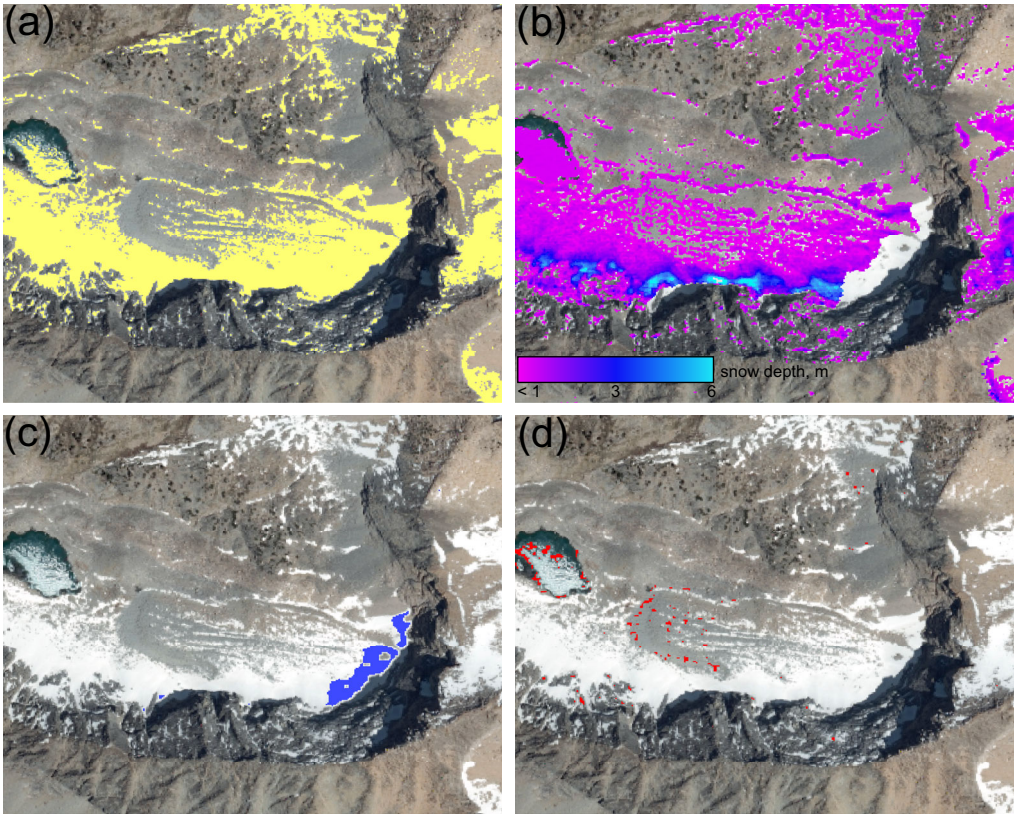

Figure 9. ASO snow cover compared to WorldView-3 imagery on 31 May 2015 in a selected area of the Kings River Basin. Shown are: (a) WorldView positives for snow in yellow; (b) ASO snow depth; (c) ASO false negatives for snow using best of a 3 × 3 neighborhood, blue; and (d) ASO false positives for snow, red. The background image is the upscaled RGB WorldView imagery.

Figures 9a–9d show one of the few areas where they do not agree. WorldView shows snow that ASO missed under and on the north and northwest facing steep rocky areas (false negatives, Figure 9c). This area was covered by snow during the summer 2014 ASO flight, but the following extremely dry year resulted in less snow on the ground in spring 2015 than during the previous summer, giving a negative SWE value; thus it was mapped as snow free. This error is indicative of problems with the ASO altimetry approach in areas with semipermanent snow fields or glaciers.

Careful visual inspection of both methods (Figures 9a and 9b) shows that snow was missed by both methods in the shadows. False positives (Figure 9d) for snow are on a partially ice-covered lake and at the edges of areas with continuous snow cover, both of which present challenges to classify at any resolution. Allowing for the locational uncertainty of the WorldView imagery, the comparison done here suggests that the snow cover measurements from ASO are accurate.

6. Conclusion

Two SWE reconstruction models, a full energy balance (EB) and net radiation/degree-day (DD) model, were verified with ASO measurements, a novel data set of fine-resolution snow measurements in the upper Tuolumne River Basin, in water years 2013–2015. SWE estimates from snow pillow interpolation and SNODAS were also compared with ASO. On average, our EB reconstruction model had no bias (0%) and low (26%) mean absolute error. The DD reconstruction model was slightly less accurate (+5% bias and 28% MAE). Large differences in the models in longwave radiation emitted from the snowpack resulted from lower modeled snow surface temperature in the EB model and slight differences in the net turbulent transfer energy. Further verification of the snowpack surface temperatures produced by the EB model is needed.

The EB reconstruction model performed slightly better than interpolation from snow pillows, and both reconstruction models performed far better than SNODAS, which overestimated SWE every year. The major advantage of the EB reconstruction model is that it relies on remotely sensed information only; it can run without ground-based measurements outside the U.S. using the Global Data Assimilation System (GLDAS) [*Rodell et al*., 2004] instead of NLDAS forcings. In comparison, SNODAS and interpolation from snow pillows rely on ground-based observations. Analysis of errors in the EB reconstruction model indicates they arise from errors in the NLDAS forcing data, signifying that other forcing data sets should be evaluated, for example CERES SYN [*Hinkelman et al*., 2015]. The remotely sensed MODSCAG/MODDRFS albedo estimates showed a near zero bias (−0.01) when compared with limited in situ measurements and were more accurate than the age-based models, which require knowledge of each snowfall. Further verification of the remotely sensed albedo estimates is needed.

Appendix A: Full Melt Model Equations

A1. Shortwave Radiation

We model downscaled shortwave radiation similarly to methods that *Rittger et al*. [2016] use, with a few differences. Incoming solar $S_\downarrow$ is by separated into beam $B_\downarrow$ and diffuse components $D_\downarrow$

$$S_\downarrow = B_\downarrow + D_\downarrow \tag{A1}$$

using empirical relationships [*Erbs et al*., 1982; *Olyphant*, 1984] based on transmittance T,

$$T = \frac{S_\downarrow}{\mu_0 S_0} \tag{A2}$$

μ_0 is the cosine of the exoatmospheric (unrefracted) solar zenith angle and S_0 is exoatmospheric irradiance. The direct solar radiation is then scaled by elevation z

$$B_\downarrow(z) = \mu_{0,r} S_0 e^{-\tau_z m} \tag{A3}$$

where $\mu_{0,r}$ is the cosine of the solar zenith angle at the surface corrected for refraction, m is the air mass [*Kasten and Young*, 1989], and τ_z is the optical depth at elevation z,

$$\tau_z = \frac{P_z}{P}\tau \tag{A4}$$

P is the reference (NLDAS) atmospheric pressure, P_z the reference pressure adjusted using a standard temperature lapse rate (−6.5 K/km) [*Lundquist and Cayan*, 2007] and the elevation difference between the reference and the fine scale elevation model. The optical depth τ is

$$\tau = \frac{-\ln T}{m} \tag{A5}$$

Then, the terrain-corrected direct solar radiation $B_{t\downarrow}$ is computed using an elevation correction. $B_\downarrow(z)$ is scaled by the cosine of the local solar zenith angle μ, along with a binary shadowing mask δ computed from local horizon angles:

$$B_{t\downarrow} = \delta \mu B_\downarrow(z) \tag{A6}$$

Terrain-corrected diffuse radiation $D_{t\downarrow}$ is also corrected by elevation using an empirical formula [*Dubayah and Loechel*, 1997] and scaled by the view factor V_d, the fraction of the overlying hemisphere that is not obstructed by terrain [*Dozier and Frew*, 1990]:

$$D_{t\downarrow} = D_\downarrow(z) V_d \tag{A7}$$

The terrain-corrected beam and diffuse radiation are then further adjusted for the tree-covered fractions of each pixel, i.e., *cc*, using a canopy extinction u_c and transmissivity τ_c [*Marks et al*., 1999; *Garen and Marks*, 2005]:

$$B_{c\downarrow} = cc B_{t\downarrow} e^{-u_c h/\mu_{0,r}} + (1-cc) B_{t\downarrow} \tag{A8}$$

$B_{c\downarrow}$ is the canopy-corrected direct radiation and h is the canopy height. Values for h, τ_c, and u_c were set according the predominant NLCD tree type, with deciduous trees having h=12 m, τ_c=0.60, and u_c=0.016 m^{-1} and coniferous trees having h=16 m, τ_c=0.30, and u_c=0.033 m^{-1} [*Garen and Marks*, 2005]. The canopy-corrected diffuse radiation is

$$D_{c\downarrow} = ccD_{t,r\downarrow}\tau_c + (1-cc)D_{t,r\downarrow} \tag{A9}$$

$D_{t,r\downarrow}$ is the terrain and reflection-corrected diffuse radiation

$$D_{t,r\downarrow} = D_{t\downarrow} + D_{r\downarrow} \tag{A10}$$

$D_{r\downarrow}$ is reflected radiation from adjacent terrain

$$D_{r\downarrow} = C_t\alpha\left[D_{t\downarrow}(1-V_d) + B_{t\downarrow}\right] \tag{A11}$$

C_t is a terrain configuration factor [*Dozier and Frew*, 1990]

$$C_t = \frac{1+\cos\vartheta}{2} - V_d; \tag{A12}$$

ϑ is the slope of the local terrain.

Using snow albedo α in equation (A11) assumes that surrounding terrain is covered by snow, which is obviously not always true. In any case, terrain-reflected solar radiation is usually small (<20 W m^{-2}). At the 500 m scale, 90% of V_d values are above 0.9, but occasional values go as low as 0.4. Given that the mixed-pixel albedo is unknown, we suggest using α provides an upper bound for terrain-reflected radiation.

A2. Longwave Radiation

Incoming longwave $I_{\downarrow}$ is modeled as the sum of incoming longwave from the atmosphere $I_{a\downarrow}$ and from surrounding terrain $I_{t\downarrow}$:

$$I_{\downarrow} = I_{a\downarrow} + I_{t\downarrow} \tag{A13}$$

with

$$I_{a\downarrow} = V_d\varepsilon_a\sigma T_a^4 \tag{A14}$$

ε_a is the atmospheric emissivity downscaled from reference estimates (NLDAS), σ is the Stefan-Boltzmann constant 5.6704×10^{-8} W m^{-2} K^{-4}, and T_a is the air temperature in Kelvin, which like P_z, was computed using a standard temperature lapse rate and the difference between the reference and the fine scale elevation model. Further

$$I_{t\downarrow} = C_t\varepsilon_s\sigma T_s^4 \tag{A15}$$

ε_S is the emissivity of snow, assumed to be 0.99 [*Dozier and Warren*, 1982], and T_s is the snow surface temperature. The incoming longwave is then adjusted for the canopy using an empirical approach [*Garen and Marks*, 2005] based on canopy cover:

$$I_{c\downarrow} = cc\left[\tau_c I_{t\downarrow} + (1-\tau_c)\varepsilon_c\sigma T_s^4\right] + (1-cc)I_{t\downarrow} \tag{A16}$$

$I_{c\downarrow}$ is the vegetation-adjusted incoming longwave radiation, and ε_c=0.98 is the emissivity of the canopy. Outgoing longwave radiation is the sum of the Stefan-Boltzmann radiation for snow plus the small fraction of the incoming longwave radiation that is reflected:

$$I_{\uparrow} = \varepsilon_s\sigma T_s^4 + (1-\varepsilon_s)I_{\downarrow} \tag{A17}$$

A3. Sensible and Latent Heat

Fluxes of sensible heat H and latent heat L are [*Liston*, 1995]

$$H = \rho_a C_p D_h \zeta (T_a - T_s) \tag{A18}$$

and

$$L=\rho_a\lambda_{v,s}D_\lambda\zeta\left(\theta\frac{e_a-e_s}{P_z}\right) \tag{A19}$$

ρ_a is the density of air; C_p is the specific heat of air at constant pressure; $D_{h,\lambda}$ are exchange coefficients for sensible and latent heat, respectively; ζ is a nondimensional stability function; θ=0.622 is the ratio of the molecular weights of water to air, and $e_{a,s}$ are the vapor pressures of air and the saturation vapor pressure at the snow surface, respectively. The enthalpy of vaporization or sublimation of water/ice $\lambda_{v,s}$ depends on e_a and e_s. For $e_s < e_a$, the enthalpy of vaporization is used; otherwise, the enthalpy of sublimation is used. The exchange coefficients $D_{h,e}$ are

$$D_{h,\lambda}=\frac{\kappa^2 u_r}{\left[\ln\left(z_r/z_0\right)\right]^2} \tag{A20}$$

with κ=0.4 as Von Karman's constant, u_r as the wind speed at reference height z_r, and z_0 as the roughness height. In this study, z_r=10 m, based on NLDAS wind speeds, and z_0=0.5 mm, a reasonable approximation for snow [*Brock et al*., 2006]. Wind speeds were downscaled using resampled NLDAS estimates, adjusted for terrain curvature, wind slope, and the canopy [*Liston and Elder*, 2006; *Liston et al*., 2007]. The curvature length scale, wind curvature and slope weighting factors were set at 2000 m (consistent with the 500 m pixel size), 0.58, and 0.42, respectively [*Liston and Elder*, 2006]. The saturation vapor pressure over ice $e_s(T_s)$ is from an empirical approximation [*Bohren and Albrecht*, 1998]. The air vapor pressure e_a is given as [*Peixoto and Oort*, 1996]:

$$e_a=q\frac{P_z}{\theta} \tag{A21}$$

with q as the specific humidity from NLDAS. For unstable atmospheric conditions $(T_s > T_a)$, the stability function ζ is

$$\zeta=1-\frac{\eta R_i}{1+\gamma\sqrt{|R_i|}} \tag{A22}$$

R_i is the Richardson number, given by

$$R_i=\frac{gz_r(T_a-T_s)}{T_a u_r^2} \tag{A23}$$

where g is gravity and γ is

$$\gamma=\varphi\eta\frac{D_{h,e}}{u_r}\sqrt{\frac{z_r}{z_0}} \tag{A24}$$

with η=9.4 and φ=5.3. For stable atmospheric conditions $(T_s < T_a)$, the stability function ζ is

$$\zeta=(1+\eta^* R_i) \tag{A25}$$

where $\eta^*=\eta/2$. For neutral conditions $(T_s=T_a)$, ζ=1.

A4. Snowpack Surface Temperature

The model solves the energy balance at each time step for snow surface T_s using the Newton-Raphson method. Equation (6) is arranged as

$$R(T_s)+H(T_s)+L(T_s)=0 \tag{A26}$$

and solved iteratively for T_s. Solutions with $T_s > 273.15$ K indicate $M_p > 0$. For that case, T_s is set to 273.15 K and M_p is computed; otherwise $M_p = 0$.

Appendix B: Error Statistics

Error statistics used include the Root-Mean-Squared Error *RMSE*,

$$RMSE = \sqrt{\frac{1}{N}\sum_{i=1}^{N}(\hat{y}_i - y_i)^2} \tag{B1}$$

Bias,

$$Bias = \frac{1}{N}\sum_{i=1}^{N}(\hat{y}_i - y_i) \tag{B2}$$

and the mean absolute error (*MAE*),

$$MAE = \frac{1}{N}\sum_{i=1}^{N}|\hat{y}_i - y_i| \tag{B3}$$

$\hat{y}$ is the modeled variable and y is the variable used for verification. These metrics were then normalized to the ASO basin-wide measured SWE for each date and reported as percentages. *RMSE* and *bias* were used to evaluate energy balance forcings while *MAE* and *bias* were used to evaluate modeled f_{SCA} and SWE. *RMSE* weights model values that are further from the measured values more heavily than *MAE*. Thus, we suggest *RMSE* is more appropriate for diagnosing errors in forcings, where errors can propagate and verification data are directly measured, while *MAE* is more appropriate for the f_{SCA} and SWE values, where verification is from modeled values, i.e., ASO SWE is modeled, not directly measured.

For binary comparisons, a 2 $\times$ 2 contingency table was created. The scalar metrics [*Doswell et al.*, 1990; *Olson and Delen*, 2008] computed from this contingency table are based on the correct and erroneous detections of snow or its absence. *TP* is a true positive (snow detected in a snow-covered pixel); *FP* is a false positive (snow detected in a pixel with no snow); *TN* is a true negative (snow not detected in a pixel with no snow); and *FN* is a false negative (snow not detected in a snow-covered pixel). The *Precision*, also called probability of detection, is

$$Precision = \frac{TP}{TP+FP} \tag{B4}$$

Recall, also called frequency of hits, is

$$Recall = \frac{TP}{TP+FN} \tag{B5}$$

Accuracy is

$$Accuracy = \frac{TP+TN}{TP+TN+FP+FN} \tag{B6}$$

The *F* score equally weights *Precision* and *Recall*:

$$F = 2\frac{Precision \times Recall}{Precision + Recall} \tag{B7}$$

Notation

a_r	degree-day factor, mm d^{-1} $^\circ C^{-1}$.
$B_\downarrow$	incoming direct solar radiation, $\frac{W}{m^2}$.
$B_\downarrow(z)$	elevation-adjusted direct solar radiation, $\frac{W}{m^2}$.
$B_{c\downarrow}$	canopy-corrected direct solar radiation, $\frac{W}{m^2}$.
$B_{t\downarrow}$	terrain-corrected direct solar radiation, $\frac{W}{m^2}$.
cc	static fractional canopy cover, dimensionless.
C_p	specific heat of air, $\frac{J}{kg\ deg}$.

C_t	terrain configuration factor, dimensionless.
$D_{\downarrow}$	incoming diffuse solar radiation, $\frac{W}{m^2}$.
$D_{\downarrow}(z)$	elevation-corrected diffuse solar radiation, $\frac{W}{m^2}$.
D_h	sensible heat exchange coefficient, $\frac{m}{s}$.
$D_{c\downarrow}$	canopy-corrected diffuse solar radiation, $\frac{W}{m^2}$.
$D_{t\downarrow}$	terrain-corrected diffuse solar radiation, $\frac{W}{m^2}$.
D_{λ}	latent heat exchange coefficient, $\frac{m}{s}$.
e_a	vapor pressure of air, Pa.
e_s	vapor pressure at snow surface, Pa.
$f_{SCA,\ raw}$	fractional snow-covered area, unadjusted, dimensionless.
f_{SCA}	fractional snow-covered area, adjusted for static canopy cover, dimensionless.
g	acceleration due to gravity, $\frac{m}{s^2}$.
G	heat flux in/out of the snowpack, assumed $\approx$0, $\frac{W}{m^2}$.
h	canopy height, m.
H	sensible heat flux, $\frac{W}{m^2}$.
$I_{\uparrow}$	outgoing longwave radiation, $\frac{W}{m^2}$.
$I_{\downarrow}$	incoming longwave radiation, $\frac{W}{m^2}$.
$I_{a\downarrow}$	incoming longwave radiation from the atmosphere, $\frac{W}{m^2}$.
$I_{c\downarrow}$	canopy-corrected incoming longwave radiation, $\frac{W}{m^2}$.
$I_{t\downarrow}$	incoming longwave radiation from surrounding terrain, $\frac{W}{m^2}$.
L	latent heat flux, $\frac{W}{m^2}$.
m	relative optical air mass, dimensionless.
m_f	melt factor, $mm\ \ water / \frac{W}{m^2}$.
M	melt, mm.
M_p	potential melt, mm.
P	atmospheric pressure, Pa.
P_z	elevation-adjusted atmospheric pressure, Pa.
q	specific humidity, dimensionless.
R	radiative heat flux, $\frac{W}{m^2}$.
R_i	Richardson number, dimensionless.
$S_{\downarrow}$	broadband incoming solar radiation, $\frac{W}{m^2}$.
S_0	exoatmospheric solar radiation, $\frac{W}{m^2}$.
T	atmospheric transmittance, dimensionless.
T_a	air temperature, K.
u_c	canopy extinction coefficient, m^{-1}.
u_r	wind speed at reference height, $\frac{m}{s}$.
V_d	view factor, dimensionless.
z_0	roughness length for snow, m.
z_r	reference height, m.
α	snow albedo, corrected for light absorbing impurities, dimensionless.
α_{clean}	clean snow albedo, dimensionless.
δ	binary shadow mask, dimensionless.
Δ_{vis}	visible wavelength snow albedo reduction from light absorbing impurities, dimensionless.
ε_a	atmospheric emissivity, dimensionless.
ε_c	emissivity of the canopy, dimensionless.
ε_s	snow emissivity, dimensionless.
ζ	nondimensional stability function, dimensionless.
θ	ratio, molecular weight of water to dry air, dimensionless.
κ	Von Karman constant, dimensionless.
$\lambda_{v,s}$	enthalpy of vaporization or sublimation of water/ice, $\frac{J}{kg}$.
μ	terrain-corrected cosine of the illumination angle, dimensionless.
μ_0	cosine of the exoatmospheric solar zenith angle.
$\mu_{0,r}$	cosine of the solar zenith angle, refracted by the atmosphere.
ρ_a	density of air, $\frac{kg}{m^3}$.

ρ_w	density of water, $\frac{kg}{m^3}$.
σ	Stefan-Boltzmann constant, W m^{-2} K^{-4}.
τ_c	canopy transmittance, dimensionless.
τ_z	elevation-adjusted optical depth, dimensionless.
τ_z	optical depth, corrected for elevation, dimensionless.
ϑ	slope angle, °.

Acknowledgments
We thank Kat Bormann and McKenzie Skiles for supplying ASO snow depth and SWE measurements at the native 3 m resolution (SWE at 50 m resolution can be downloaded from http://aso.jpl.nasa.gov/). We thank Jessica Lundquist, Manuela Girotto, Noah Molotch, and an anonymous reviewer for their constructive reviews. Support for this work comes from the U.S. Army Cold Regions Research and Engineering Laboratory Award W913E5-15-C-0003, NASA Awards NNH11ZDA001N and NNX12AJ87G, and Microsoft Research. Part of this work was performed at the Jet Propulsion Laboratory, California Institute of Technology under a contract with NASA. All data and software used in this study are available either through the links in the text or upon request. We are currently working with the UCSB Library on their initiative to serve data from investigations carried out by researchers on campus.

References

Bair, E., J. Dozier, R. E. Davis, M. T. Colee, and K. J. Claffey (2015), CUES—A study site for measuring snowpack energy balance in the Sierra Nevada, *Frontiers Earth Sci.*, *3*, doi:10.3389/feart.2015.00058.
Barrett, A. (2003), National Operational Hydrologic Remote Sensing Center SNOw Data Assimiliation System (SNODAS) products at NSIDC, *Spec. Rep. 11*, 19 pp., Natl. Snow and Ice Data Cent., Boulder, Colo.
Bay Area Water Supply and Conservation Agency (2015), Hetch Hetchy Water System, San Mateo, Calif. [Available at http://bawsca.org/water-supply/hetch-hetchy-water-system/.]
Bohren, C. F., and B. A. Albrecht (1998), *Atmospheric Thermodynamics*, 402 pp., Oxford Univ. Press, New York, N. Y.
Brock, B. W., I. C. Willis, and M. J. Sharp (2006), Measurement and parameterization of aerodynamic roughness length variations at Haut Glacier d'Arolla, Switzerland, *J. Glaciol.*, *52*, 281–297, doi:10.3189/172756506781828746.
Brubaker, K., A. Rango, and W. Kustas (1996), Incorporating radiation inputs into the snowmelt runoff model, *Hydrol. Processes*, *10*, 1329–1343, doi:10.1002/(SICI)1099-1085(199610)10:10 < 1329::AID-HYP464 > 3.0.CO;2-W.
Burt, P., and E. Adelson (1983), The Laplacian pyramid as a compact image code, *IEEE Trans. Commun.*, *31*, 532–540, doi:10.1109/TCOM.1983.1095851.
Cline, D. W., R. C. Bales, and J. Dozier (1998), Estimating the spatial distribution of snow in mountain basins using remote sensing and energy balance modeling, *Water Resour. Res.*, *34*, 1275–1285, doi:10.1029/97WR03755.
Clow, D. W., L. Nanus, K. L. Verdin, and J. Schmidt (2012), Evaluation of SNODAS snow depth and snow water equivalent estimates for the Colorado Rocky Mountains, USA, *Hydrol. Processes*, *26*, 2583–2591, doi:10.1002/hyp.9385.
Cosgrove, B. A., et al. (2003), Real-time and retrospective forcing in the North American Land Data Assimilation System (NLDAS) project, *J. Geophys. Res.*, *108*(D22), 8842, doi:10.1029/2002JD003118.
Davis, R. E., R. E. Jordan, S. Daly, and G. G. Koenig (2001), Validation of snow models, in *Model Validation: Perspectives in Hydrological Science*, edited by M. G. Anderson and P. D. Bates, pp. 261–292, John Wiley, New York.
Dickinson, R. E., A. Henderson-Sellers, and P. J. Kennedy (1993), Biosphere-Atmosphere Transfer Scheme (BATS) Version 1e as coupled to the NCAR Community Climate Model, *Tech. Note NCAR/TN-387+STR*, 72 pp., Natl. Cent. for Atmos. Res., Boulder, Colo.
Doswell, C. A., R. Davies-Jones, and D. L. Keller (1990), On summary measures of skill in rare event forecasting based on contingency tables, *Weather Forecasting*, *5*, 576–585, doi:10.1175/1520-0434(1990)005 < 0576:OSMOSI>2.0.CO;2.
Dozier, J. (1989), Spectral signature of alpine snow cover from the Landsat Thematic Mapper, *Remote Sens. Environ.*, *28*, 9–22, doi:10.1016/0034-4257(89)90101-6.
Dozier, J. (2011), Mountain hydrology, snow color, and the fourth paradigm, *Eos Trans. AGU*, *92*, 373–375, doi:10.1029/2011EO430001.
Dozier, J., and J. Frew (1990), Rapid calculation of terrain parameters for radiation modeling from digital elevation data, *IEEE Trans. Geosci. Remote Sens.*, *28*, 963–969, doi:10.1109/36.58986.
Dozier, J., and S. G. Warren (1982), Effect of viewing angle on the infrared brightness temperature of snow, *Water Resour. Res.*, *18*, 1424–1434, doi:10.1029/WR018i005p01424.
Dozier, J., T. H. Painter, K. Rittger, and J. E. Frew (2008), Time-space continuity of daily maps of fractional snow cover and albedo from MODIS, *Adv. Water Resour.*, *31*, 1515–1526, doi:10.1016/j.advwatres.2008.08.011.
Dozier, J., E. H. Bair, and R. E. Davis (2016), Estimating the spatial distribution of snow water equivalent in the world's mountains, *WIREs Water*, *3*, 461–474, doi:10.1002/wat2.1140.
Dubayah, R., and S. Loechel (1997), Modeling topographic solar radiation using GOES data, *J. Appl. Meteorol.*, *36*, 141–154, doi:10.1175/1520-0450(1997)036 < 0141:MTSRUG>2.0.CO;2.
Durand, M., N. P. Molotch, and S. A. Margulis (2008), Merging complementary remote sensing datasets in the context of snow water equivalent reconstruction, *Remote Sens. Environ.*, *112*, 1212–1225, doi:10.1016/j.rse.2007.08.010.
Erbs, D. G., S. A. Klein, and J. A. Duffie (1982), Estimation of the diffuse radiation fraction for hourly, daily and monthly-average global radiation, *Solar Energy*, *28*, 293–302, doi:10.1016/0038-092X(82)90302-4.
Farr, T. G., et al. (2007), The Shuttle Radar Topography Mission, *Rev. Geophys.*, *45*, RG2004, doi:10.1029/2005RG000183.
Fassnacht, S. R., K. A. Dressler, and R. C. Bales (2003), Snow water equivalent interpolation for the Colorado River Basin from snow telemetry (SNOTEL) data, *Water Resour. Res.*, *39*(8), 1208, doi:10.1029/2002WR001512.
Gardner, A. S., and M. J. Sharp (2010), A review of snow and ice albedo and the development of a new physically based broadband albedo parameterization, *J. Geophys. Res.*, *115*, F01009, doi:10.1029/2009JF001444.
Garen, D. C., and D. Marks (2005), Spatially distributed energy balance snowmelt modelling in a mountainous river basin: Estimation of meteorological inputs and verification of model results, *J. Hydrol.*, *315*, 126–153, doi:10.1016/j.jhydrol.2005.03.026.
Girotto, M., S. A. Margulis, and M. Durand (2014), Probabilistic SWE reanalysis as a generalization of deterministic SWE reconstruction techniques, *Hydrol. Processes*, *28*, 3875–3895, doi:10.1002/hyp.9887.
Glassner, A. S. (Ed.) (1993), *Graphics Gems*, 864 pp., Academic, New York.
Guan, B., N. P. Molotch, D. E. Waliser, S. M. Jepsen, T. H. Painter, and J. Dozier (2013), Snow water equivalent in the Sierra Nevada: Blending snow sensor observations with snowmelt model simulations, *Water Resour. Res.*, *49*, 5029–5046, doi:10.1002/wrcr.20387.
Gueymard, C. A. (2004), The sun's total and spectral irradiance for solar energy applications and solar radiation models, *Solar Energy*, *76*, 423–453, doi:10.1016/j.solener.2003.08.039.
Hall, D. K., V. V. Salomonson, and G. A. Riggs (2006), *MODIS/Terra Snow Cover Daily L3 Global 500 m Grid, Fractional Snow Covered Area*, Natl. Snow and Ice Data Cent., Boulder, Colo., doi:10.5067/63NQASRDPDB0.
Hastie, T., R. Tibshirani, and J. Friedman (2009), *The Elements of Statistical Learning: Data Mining, Inference, and Prediction*, 2nd ed., 745 pp., Springer, Berlin.

Hinkelman, L. M., K. E. Lapo, N. C. Cristea, and J. D. Lundquist (2015), Using CERES SYN surface irradiance data as forcing for snowmelt simulation in complex terrain, *J. Hydrometeorol.*, *16*, 2133–2152, doi:10.1175/JHM-D-14-0179.1.

Homer, C. G., J. A. Dewitz, L. Yang, S. Jin, X. P. Danielson, C. G. Xian, H. J. Coulston, N.D. Herold, J. D. Wickham, and K. Megown (2015), Completion of the 2011 National Land Cover Database for the conterminous United States-Representing a decade of land cover change information, *Photogramm. Eng. Remote Sens.*, *81*, 345–354.

Jepsen, S. M., N. P. Molotch, M. W. Williams, K. E. Rittger, and J. O. Sickman (2012), Interannual variability of snowmelt in the Sierra Nevada and Rocky Mountains, United States: Examples from two alpine watersheds, *Water Resour. Res.*, *48*, W02529, doi:10.1029/2011WR011006.

Kasten, F., and A. T. Young (1989), Revised optical air mass tables and approximation formula, *Appl. Opt.*, *28*, 4735–4738, doi:10.1364/AO.28.004735.

Kings River Conservation District (2009), *The Kings River Handbook*, 40 pp., Fresno, Calif. [Available at http://www.krcd.org/_pdf/Kings_River_Handbook_2009.pdf.]

Kustas, W. P., A. Rango, and R. Uijlenhoet (1994), A simple energy budget algorithm for the snowmelt runoff model, *Water Resour. Res.*, *30*, 1515–1527, doi:10.1029/94wr00152.

Landry, C. C., K. A. Buck, M. S. Raleigh, and M. P. Clark (2014), Mountain system monitoring at Senator Beck Basin, San Juan Mountains, Colorado: A new integrative data source to develop and evaluate models of snow and hydrologic processes, *Water Resour. Res.*, *50*, 1773–1788, doi:10.1002/2013WR013711.

Lettenmaier, D. P., D. Alsdorf, J. Dozier, G. J. Huffman, M. Pan, and E. F. Wood (2015), Inroads of remote sensing into hydrologic science during the WRR era, *Water Resour. Res.*, *51*, 7309–7342, doi:10.1002/2015WR017616.

Liang, X., D. P. Lettenmaier, E. F. Wood, and S. J. Burges (1994), A simple hydrologically based model of land surface water and energy fluxes for general circulation models, *J. Geophys. Res.*, *99*, 14,415–14,428, doi:10.1029/94JD00483.

Liston, G. E. (1995), Local advection of momentum, heat, and moisture during the melt of patchy snow covers, *J. Appl. Meteorol.*, *34*, 1705–1715, doi:10.1175/1520-0450-34.7.1705.

Liston, G. E., and K. Elder (2006), A meteorological distribution system for high-resolution terrestrial modeling (MicroMet), *J. Hydrometeorol.*, *7*, 217–234, doi:10.1175/JHM486.1.

Liston, G. E., R. B. Haehnel, M. Sturm, C. A. Hiemstra, S. Berezovskaya, and R. D. Tabler (2007), Simulating complex snow distributions in windy environments using SnowTran-3D, *J. Glaciol.*, *53*, 241–256, doi:10.3189/172756507782202865.

López-Moreno, J. I., S. R. Fassnacht, J. T. Heath, K. N. Musselman, J. Revuelto, J. Latron, E. Morán-Tejeda, and T. Jonas (2013), Small scale spatial variability of snow density and depth over complex alpine terrain: Implications for estimating snow water equivalent, *Adv. Water Resour.*, *55*, 40–52, doi:10.1016/j.advwatres.2012.08.010.

Lundquist, J. D., and D. R. Cayan (2007), Surface temperature patterns in complex terrain: Daily variations and long-term change in the central Sierra Nevada, California, *J. Geophys. Res.*, *112*, D11124, doi:10.1029/2006JD007561.

Marks, D., and J. Dozier (1992), Climate and energy exchange at the snow surface in the alpine region of the Sierra Nevada: 2. Snow cover energy balance, *Water Resour. Res.*, *28*, 3043–3054, doi:10.1029/92wr01483.

Marks, D., J. Domingo, D. Susong, T. Link, and D. Garen (1999), A spatially distributed energy balance snowmelt model for application in mountain basins, *Hydrol. Processes*, *13*, 1935–1959, doi:10.1002/(SICI)1099-1085(199909)13:12/13 < 1935::AID-HYP868 > 3.0.CO;2-C.

Martinec, J., and A. Rango (1981), Areal distribution of snow water equivalent evaluated by snow cover monitoring, *Water Resour. Res.*, *17*, 1480–1488, doi:10.1029/WR017i005p01480.

McGurk, B. J., and T. H. Painter (2014), Airborne Snow Observatory: Hetch Hetchy Basin snow water equivalent time series, 2013, in *82nd Western Snow Conference*, pp. 173–176, Durango, Colo. [Available at http://westernsnowconference.org/node/1754.]

Molotch, N. P. (2009), Reconstructing snow water equivalent in the Rio Grande headwaters using remotely sensed snow cover data and a spatially distributed snowmelt model, *Hydrol. Processes*, *23*, 1076–1089, doi:10.1002/hyp.7206.

Molotch, N. P., and R. C. Bales (2005), Scaling snow observations from the point to the grid element: Implications for observation network design, *Water Resour. Res.*, *41*, W11421, doi:10.1029/2005WR004229.

Molotch, N. P., and R. C. Bales (2006), Comparison of ground-based and airborne snow surface albedo parameterizations in an alpine watershed: Impact on snowpack mass balance, *Water Resour. Res.*, *42*, W05410, doi:10.1029/2005WR004522.

Molotch, N. P., and S. A. Margulis (2008), Estimating the distribution of snow water equivalent using remotely sensed snow cover data and a spatially distributed snowmelt model: A multi-resolution, multi-sensor comparison, *Adv. Water Resour.*, *31*, 1503–1514, doi:10.1016/j.advwatres.2008.07.017.

Molotch, N. P., S. A. Margulis, and S. M. Jepsen (2010), Response to comment by A.G. Slater, M.P. Clark, and A.P. Barrett on 'Estimating the distribution of snow water equivalent using remotely sensed snow cover data and a spatially distributed snowmelt model: A multi-resolution, multi-sensor comparison' [[Adv Water Resour 31 (2008) 1503-1514]. Adv Water Resour 2009;32(11):1680-4], *Adv. Water Resour.*, *33*, 231–239, doi:10.1016/j.advwatres.2009.11.008.

Musselman, K. N., J. W. Pomeroy, R. L. H. Essery, and N. Leroux (2015), Impact of windflow calculations on simulations of alpine snow accumulation, redistribution and ablation, *Hydrol. Processes*, *29*, 3983–3999, doi:10.1002/hyp.10595.

NSIDC (2016), *Snow Data Assimilation System (SNODAS) Data Products at NSIDC*, Natl. Snow and Ice Data Cent., Boulder, Colo., doi:10.7265/N5TB14TC.

Okabe, A., B. Boots, K. Sugihara, and S. N. Chiu (2000), *Spatial Tessellations: Concepts and Applications of Voronoi Diagrams*, 696 pp., John Wiley, New York.

Olson, D. L., and D. Delen (2008), *Advanced Data Mining Techniques*, 180 pp., Springer, Berlin.

Olyphant, G. A. (1984), Insolation topoclimates and potential ablation in alpine snow accumulation basins: Front Range, Colorado, *Water Resour. Res.*, *20*, 491–498, doi:10.1029/WR020i004p00491.

Outcalt, S. I., C. Goodwin, G. Weller, and J. Brown (1975), Computer simulation of the snowmelt and soil thermal regime at Barrow, Alaska, *Water Resour. Res.*, *11*, 709–715, doi:10.1029/WR011i005p00709.

Painter, T. H., K. Rittger, C. McKenzie, P. Slaughter, R. E. Davis, and J. Dozier (2009), Retrieval of subpixel snow-covered area, grain size, and albedo from MODIS, *Remote Sens. Environ.*, *113*, 868–879, doi:10.1016/j.rse.2009.01.001.

Painter, T. H., A. C. Bryant, and S. M. Skiles (2012), Radiative forcing by light absorbing impurities in snow from MODIS surface reflectance data, *Geophys. Res. Lett.*, *39*, L17502, doi:10.1029/2012GL052457.

Painter, T. H., F. C. Seidel, A. C. Bryant, S. M. Skiles, and K. Rittger (2013), Imaging spectroscopy of albedo and radiative forcing by light-absorbing impurities in mountain snow, *J. Geophys. Res. Atmos.*, *118*, 9511–9523, doi:10.1002/jgrd.50520.

Painter, T. H., et al. (2016), The Airborne Snow Observatory: Fusion of scanning lidar, imaging spectrometer, and physically-based modeling for mapping snow water equivalent and snow albedo, *Remote Sens. Environ.*, *184*, 139–152, doi:10.1016/j.rse.2016.06.018.

Peixoto, J., and A. H. Oort (1996), The climatology of relative humidity in the atmosphere, *J. Clim.*, *9*, 3443–3463, doi:10.1175/1520-0442(1996)009 < 3443:TCORHI>2.0.CO;2.

Raleigh, M. S., C. C. Landry, M. Hayashi, W. L. Quinton, and J. D. Lundquist (2013a), Approximating snow surface temperature from standard temperature and humidity data: New possibilities for snow model and remote sensing evaluation, *Water Resour. Res.*, *49*, 8053–8069, doi:10.1002/2013WR013958.

Raleigh, M. S., K. Rittger, C. E. Moore, B. Henn, J. A. Lutz, and J. D. Lundquist (2013b), Ground-based testing of MODIS fractional snow cover in subalpine meadows and forests of the Sierra Nevada, *Remote Sens. Environ.*, *128*, 44–57, doi:10.1016/j.rse.2012.09.016.

Rittger, K., T. H. Painter, and J. Dozier (2013), Assessment of methods for mapping snow cover from MODIS, *Adv. Water Resour.*, *51*, 367–380, doi:10.1016/j.advwatres.2012.03.002.

Rittger, K., E. H. Bair, A. Kahl, and J. Dozier (2016), Spatial estimates of snow water equivalent from reconstruction, *Adv. Water Resour.*, *94*, 345–363, doi:10.1016/j.advwatres.2016.05.015.

Rittger, K. E. (2012), Spatial estimates of snow water equivalent in the Sierra Nevada, PhD thesis, 245 pp., Univ. of Calif., Santa Barbara.

Rodell, M., et al. (2004), The Global Land Data Assimilation System, *Bull. Am. Meteorol. Soc.*, *85*, 381–394, doi:10.1175/BAMS-85-3-381.

Rosenthal, W., and J. Dozier (1996), Automated mapping of montane snow cover at subpixel resolution from the Landsat Thematic Mapper, *Water Resour. Res.*, *32*, 115–130, doi:10.1029/95WR02718.

Slater, A. G., A. P. Barrett, M. P. Clark, J. D. Lundquist, and M. S. Raleigh (2013), Uncertainty in seasonal snow reconstruction: Relative impacts of model forcing and image availability, *Adv. Water Resour.*, *55*, 165–177, doi:10.1016/j.advwatres.2012.07.006.

Walter, M. T., E. S. Brooks, D. K. McCool, L. G. King, M. Molnau, and J. Boll (2005), Process-based snowmelt modeling: Does it require more input data than temperature-index modeling?, *J. Hydrol.*, *300*, 65–75, doi:10.1016/j.jhydrol.2004.05.002.

Wetlaufer, K., J. Hendrikx, and L. Marshall (2016), Spatial heterogeneity of snow density and its influence on snow water equivalence estimates in a large mountainous basin, *Hydrology*, *3*, 3, doi:10.3390/hydrology3010003.

Xia, Y., et al. (2012), Continental-scale water and energy flux analysis and validation for the North American Land Data Assimilation System project phase 2 (NLDAS-2): 1. Intercomparison and application of model products, *J. Geophys. Res.*, *117*, D03109, doi:10.1029/2011JD016048.